Compatible domain structures in ferroelectric single crystals

Nien-Ti Tsou
Jesus College
Department of Engineering Science
University of Oxford

Michaelmas Term 2011

Compatible domain structures in ferroelectric single crystals

Nien-Ti Tsou, Jesus College, University of Oxford
For the degree of D.Phil. in Engineering Science, Michaelmas Term 2011

Abstract

The aim of the current study is to develop an efficient model which can predict low-energy compatible microstructures in ferroelectric bulks and film devices and their dynamic behaviour. The results are expected to assist in the interpretation of microstructure observations and provide a knowledge of the possible domain arrangements that can be used to design future materials with optimum performance.

Several recent models of ferroelectric crystals assume low energy domain configurations. They are mainly based on the idea of fine phase mixtures and average compatibility, and can require intensive computation resulting in complex domain configurations which rarely occur in nature. In this research, criteria for the exact compatibility of domain structure in the form of a periodic multi-rank laminate are developed. Exactly compatible structure is expected to be energetically favourable and does not require the concept of a fine mixture to eliminate incompatibilities. The resulting method is a rapid and systematic procedure for finding exactly compatible microstructures. This is then used to explore minimum rank compatible microstructure in various crystal systems and devices. The results reveal routes in polarization and strain spaces along which microstructure can continuously evolve, including poling paths for ferroelectric single crystals. Also, the method is capable to generate all possible exactly compatible laminate configurations for given boundary conditions. It is found that simple configurations are often energetically favourable in conditions where previous approaches would predict more complex domain patterns. Laminate domain patterns in ferroelectrics are classified and correlated with observations of domains in single crystals, showing good agreement.

The evolution of microstructures under applied mechanical and electrical loads is studied. A variational method, which minimises the overall energy of the crystal is developed. A new concept of transitional "pivot states" is introduced which allows the model to capture the feature that the microstructure in ferroelectric crystal switches between possible domain patterns that are energetically favourable, rather than assuming one particular domain pattern throughout. This model is applied to study the hysteresis responses of barium titanate ($BaTiO_3$) single crystals subjected to a variety of loads. The results have good agreement with experimental data in the literature. The relationship between domain patterns and ferroelectric hysteresis responses is discussed.

Acknowledgements

I am immensely grateful to my supervisor, John Huber, for his help and support in every aspect of my life in Oxford. He is always encouraging my learning, tolerating my language skills and inspiring me with his extreme enthusiasm for research. In particular, I would like to thank him for investing his time to help me in turning our research into this thesis and several publications. Without his advice and encouragement, I would never have finished these difficult tasks.

I would like to thank Professor Alan Cocks for his advice over these four years. His genuine insights have been especially helpful in the times I have been stuck with my research. I also deeply appreciate his and Dr. Simon Gill's constructive comments and their time spent for my thesis viva. I am also grateful for the kind help from Prof. Chuin-Shan Chen, Prof. Jay Shieh and Prof. Yi-Chung Shu in National Taiwan University. They shared with me their invaluable experiences and knowledge even when I am far away in Oxford.

I thank all the members in the Solid Mechanics and Materials Engineering group for making my life in Oxford enjoyable. Especially, I want to thank Prashant Potnis for his advice regarding ferroelectric experiments as well as his useful suggestions about living in the UK when I first arrived. Many thanks to Matthew Arthington who willingly offered me all kinds of help. I would also like to thank him and Olga Barrera for constantly organising the coffee/lunch breaks that allowed me to keep connected with everyone in the group.

I deeply appreciate the generous sponsorship from EPSRC. Their support not only covered my financial burdens, but also provided many useful courses and career trainings. Also, I would like to thank my supervisor and Professor Alan Cocks again for offering me the opportunity to continue my work in the department. It has been an honour and pleasure to be a member of Jesus College, and many thanks go to Jesus College for its kind and heart-warming support, which I particularly felt as an international student.

I treasure the friendships with Dave, Thomas Brantzos, Nicolas Motz, Luby, Celeste, Ken, Jenny, Duen, Chih-Suei Shaw, Alan, Dumpling gang and all my friends who have enriched my DPhil life. I also appreciate the constant care and greetings from my friends who are not in the UK: Bruce, Meimei, Jack, Easy, Chi-Hou Lei and many others. I feel really lucky to have you guys!

Finally, I would like to give special thanks to my parents and family for their unconditional love and infinite patience. Receiving their encouragement and support through online video chats has been my mental vitamin for each week! I also want to thank my girlfriend, Lilya, who has taken such good care of me and been my source of happiness.

Contents

1

Introduction and literature review

1.1 Motivation

In recent decades, ferroelectric crystals have been widely used in many applications such as sensors, actuators and memory devices. The fundamental behaviour of these materials is strong electrical and mechanical coupling that gives the crystals an ability to sense changes of external loading or boundary conditions. Although ferroelectricity has been known since 1921, there is still a lack of systematic design process for ferroelectric devices. This is because material of this kind generally has nonlinear behaviour during operation, and the understanding of nonlinearities caused by ferroelectric microstructure is not yet complete. The microstructure plays a key role in determining the properties of the crystal and has been the subject of extensive study [1–5]; ferroelectric microstructure modelling is of interest both in academia and in industry.

A wide variety of techniques are used for modelling ferroelectric microstructure. Several of these techniques require intensive computation such as phase field models and *ab initio* models. Phase field models simulate material elements of order nanometer size and thus many elements are needed; *ab initio* models and related atomistic calculations solve quantum mechanical equations and model every atom; they are thus limited to very small regions. By contrast, sharp interface models and related large scale computations neglect the thickness of interfaces

in the microstructure and that significantly reduces the complexity. Thus the overall behaviour of a microstructure can be captured without the need for accurately modelling every detail.

Recently, phase field models [6,6–22] of ferroelectric crystals have been extensively studied and the results are well accepted. However, only a small region of a crystal can be modeled and heavy computations are needed. For engineering design purposes, we need larger scale models for better efficiency, but still want to capture the complex behaviour of ferroelectric single crystals. This motivates the current study for a continuum approach where key microstructural features are captured.

1.2 Introduction to ferroelectric crystals

Ferroelectric crystals are defined by having a spontaneous polarization, that can be reoriented by an electric field [23]. The spontaneous polarization is induced by a non-centrosymmetric crystal structure. When a ferroelectric crystal is above a critical temperature, known as Curie temperature (T_c), the crystal is in the paraelectric phase which forms a symmetric lattice structure causing no net polarization, as shown in figure 1.1(a). However, when it cools down below the Curie temperature, the central cation (Ti^{4+} in figure 1.1(b)) moves off centre and a net spontaneous polarization ($\mathbf{P}^s$) is generated. Figure 1.1 shows the phase transition from cubic to tetragonal crystal system in barium titanate ($BaTiO_3$), which is one of the commonly used ferroelectric materials.

The direction of central cation movement gives the lattice specific strain and polarization states. Figure 1.2 shows the possible polarization directions in three typical ferroelectric crystal systems. Figure 1.2(a) shows a reference cubic phase with equal lattice parameters a_0. This arrangement does not have any polarization. Tetragonal crystals have three polarization directions parallel to the edges of the unit cell, resulting in 6 crystal variants with polarization vectors directed towards the centres of the faces of a cube. The lattice deformation introduces

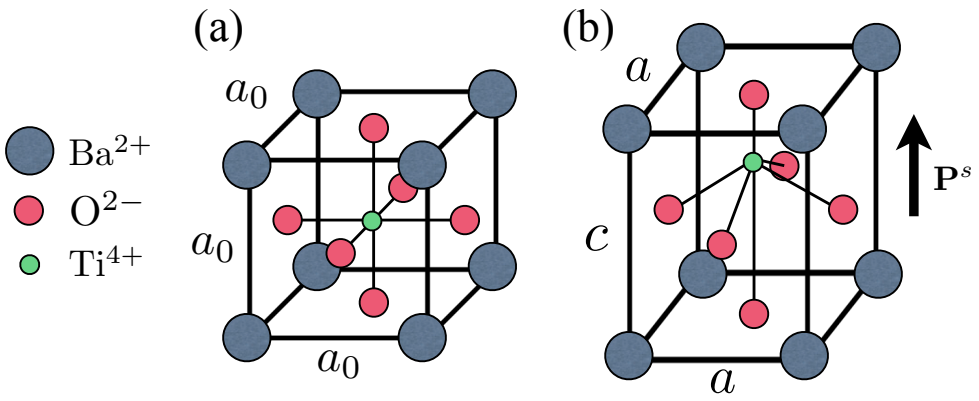

Figure 1.1: Ferroelectric lattice of barium titanate ($BaTiO_3$) with (a) paraelectric cubic phase above T_c and (b) ferroelectric tetragonal phase below T_c.

two crystal parameters a and c, as shown in figure 1.2(b). Similarly, orthorhombic crystals are polarized along the $\langle 110 \rangle$ family of directions and have 12 crystal variants with polarization vectors toward the central point of each edge in the unit cell, as shown in figure 1.2(c). Rhombohedral crystals have a spontaneous polarization in the $\langle 111 \rangle$ family of directions, resulting in 8 crystal variants with polarization vectors toward eight vertices in the unit cell respectively. The lattice has a shear strain giving a rhombohedral angle α and lattice parameters a, as shown in figure 1.2(d). These lattice structures are stable over certain temperature ranges. For example, barium titanate ($BaTiO_3$) is in a paraelectric phase with no net polarization above the Curie temperature ($T_c = 120\,^{\circ}\mathrm{C}$), but adopts a polar tetragonal phase in the temperature range $5\,^{\circ}\mathrm{C}$ to $120\,^{\circ}\mathrm{C}$. Figure 1.2 shows the various phases adopted by barium titanate over a range of temperatures [24].

A ferroelectric crystal with non-zero net polarization has the effect of piezoelectricity. There are two types of piezoelectric effect: direct and converse [23]. The elastic, dielectric and piezoelectric behaviour of the crystal can be described by:

$$D_i = d_{ikl}\sigma_{kl} + \kappa^{\sigma}_{ik}E_k \tag{1.1}$$

$$\epsilon_{ij} = s^{E}_{ijkl}\sigma_{kl} + d_{kij}E_k \tag{1.2}$$

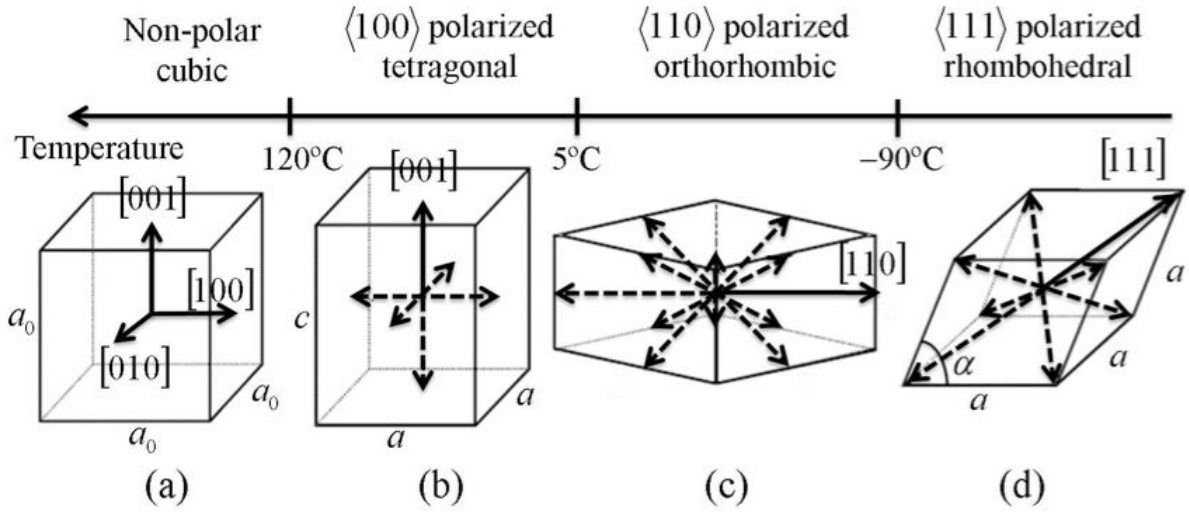

Figure 1.2: Phase transformations in barium titanate [24]. (a) cubic crystal system; (b) tetragonal system with 6 crystal variants; (c) orthorhombic system with 12 variants; (d) rhombohedral system with 8 variants.

where D_i is the electric displacement; d_{ikl} is the tensor of piezoelectric coefficients; σ_{kl} is the stress; κ_{ik}^{σ} is the dielectric constant under constant stress; E_k is the electric field; ϵ_{ij} is the strain; s_{ijkl}^{E} is the compliance under constant electric field [25]. The coefficient d_{ikl} in equation (1.1) represents the direct piezoelectric effect which indicates that stress can generate electric displacement. This effect can be used in applications such as generators and sensors. On the other hand, the converse effect is described in equation (1.2). This effect allows one to control the straining of the crystal by applying an electric field. Several applications such as actuators and motors are based on this characteristic.

So far we have only considered the unit cells of ferroelectric crystals, and how they give rise to macroscopic piezoelectricity. However, an important aspect of these crystals is their microstructure. Microscopic observation of ferroelectric crystals reveals patterned microstructure, consisting of regions known as "domains" [1]. Domains are regions with uniform spontaneous electrical polarization and lattice strain. Where domains meet, thin interfaces known as domain walls form. Domain walls with a low energy configuration are said to be compatible: they have no net charge (continuity of the normal component of electrical polarization) and no dislocations (continuity of lattice strain) [1, 24, 26]. The compatibility conditions at a single domain

wall are well known [24, 26], and give rise to particular orientations of domain wall. However, in a microstructure consisting of more than two domains, domains often form a multi-rank laminate structure, as shown in figure 1.3. This domain configuration is called a herringbone pattern [1, 2]. To minimise the energy of the structure, some subtle complications arise. For example, there are two types of domain wall in the tetragonal crystal system: 180° and 90° domain walls. Figure 1.4(a) shows a 180° domain wall separating crystal lattices with anti-parallel polarizations. These lattices have identical strain states; they can perfectly align along the interface. Figure 1.4(b) shows a 90° domain wall, across which the polarization rotates through about 90°. In this crystal system, the compatibility conditions on strain and polarization give six unique domain wall orientations for six 90° domain pairs, while domain walls for 180° domain pairs have no such habit plane, as shown in figure 1.5. The 180° domain wall structures are often observed as "watermarks" in ferroelectric crystals, as can be seen in figure 1.3 [1]. This degeneracy in domain wall orientation results in a non-unique minimum energy domain configuration.

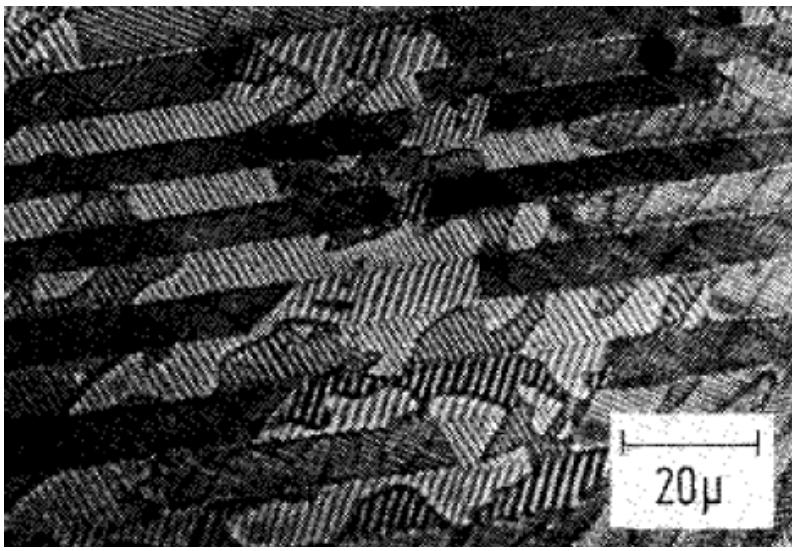

Figure 1.3: Laminate structure in herringbone pattern with watermarks formed by 180° domain wall [1].

Consider a ferroelectric crystal subjected to external loading such as an electric field. The position of positively and negatively charged ions is forced to change, and this can result in the

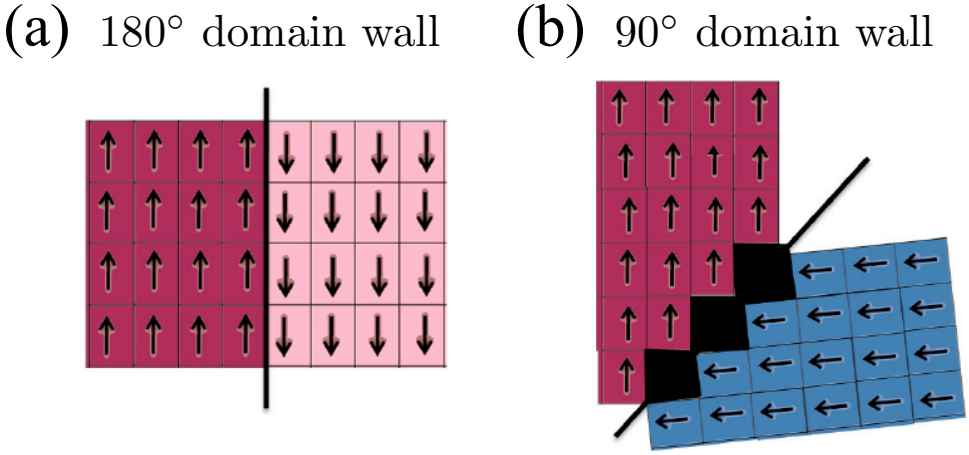

Figure 1.4: (a) A 180° domain wall separating lattices with anti-parallel polarizations. (b) A 90° domain wall.

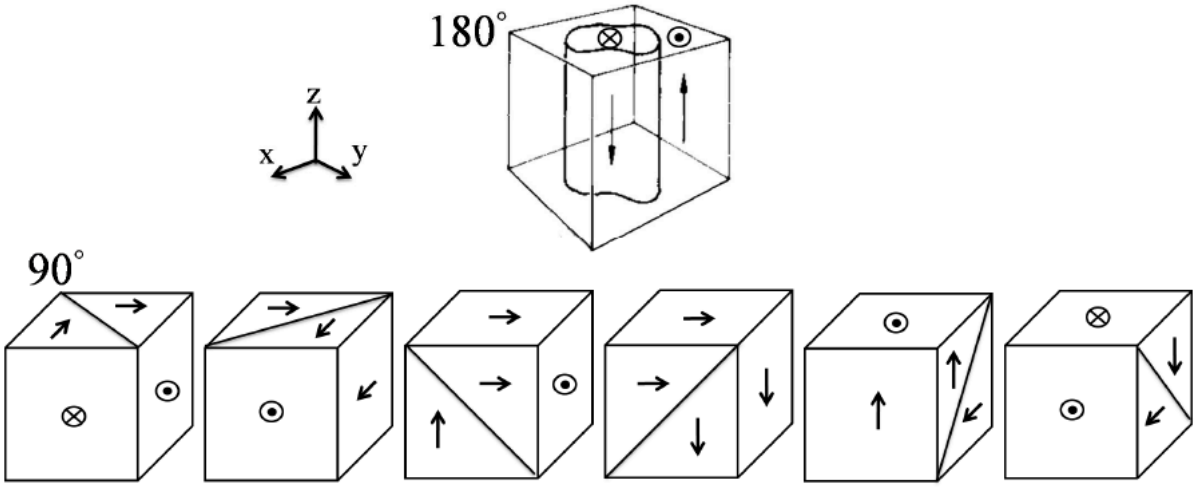

Figure 1.5: Types of domain wall orientations in the tetragonal crystal system [1].

central cation in each unit cell jumping to a new stable equilibrium configuration. This process is known as "switching" [5]. In this way, a domain can switch from one to another crystal variant. Domain wall movement is typically the microstructural mechanism of the switching process. Motion of domain walls allows the polarization to switch one atomic layer at a time, giving an incremental process for switching an entire domain [27].

When a ferroelectric crystal is just made, the process of cooling through the Curie temperature (T_c) induces spontaneous polarizations in crystallographically favoured directions, but the randomness of this process typically results in a state of zero average polarization and zero

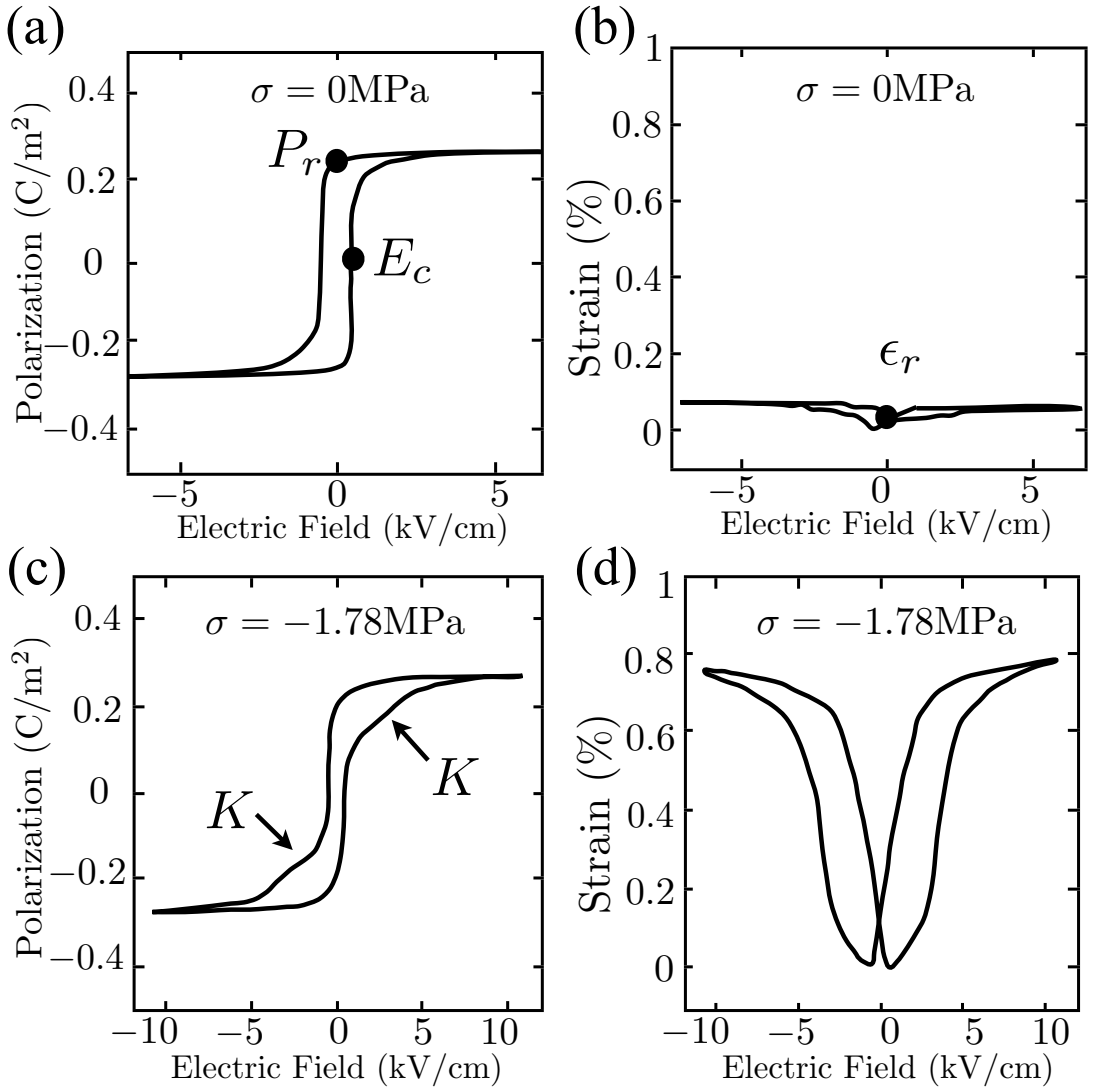

Figure 1.6: Hysteresis loops of a single crystal of $BaTiO_3$ subjected to a uniform compressive stress $\sigma_3 = 0\,\mathrm{MPa},\ -1.78\,\mathrm{MPa}$ and a cyclic electric field along z-direction. (modified from Burcsu *et al.* [28])

residual strain. In this state there is no macroscopic piezoelectric effect. However, the polarization can be aligned by applying a strong electric field. Then, net polarization and strain of the crystal are generated and effects such as piezoelectricity are also induced. This important process is known as "poling". As the polarization switches, domain structure is reorganized and the macroscopic properties are changed. By measuring the relation between electric field and macroscopic polarization or strain in the crystal, cyclic hysteresis loops can be observed, see figure 1.6.

Figure 1.6(a) and (b) show dielectric and strain hysteresis loops of a tetragonal single crystal of $BaTiO_3$ subjected to a cyclic electric field along the z-direction [28]. In figure 1.6(a), the two steep portions of the loop are due to a 180° domain switching which involves the nucleation and growth of domains which have 180° reversed polarization. When the polarization equals zero, the magnitude of the electric field is known as the coercive field (E_c). It is an important indication for ferroelectric materials that gives the required intensity of applied electric field to cause domain switching. As the magnitude of the electric field increases, the polarization reaches saturation and domain switching is complete at the tips of the loop. As the electric field is gradually removed, polarization linearly decreases to the remanent polarization (P_r) when the electric field becomes zero; the strain state at this point in figure 1.6(b) is referred to as the remanent strain (ϵ_r). Equally, the crystal has the same behaviour, but with a negative sign, when applying opposite electric field. It can be observed that there is very little strain hysteresis response in figure 1.6(b). It is because only 180° switching occurs during this process, where the polarization direction of the crystal is reversed by 180° but with no change of remanent strain state. The crystal cycles between two crystal variants with out-of-plane polarization direction without going through the crystal variants that have in-plane polarization.

However, when a uniform compressive stress $\sigma_3 = -1.78\,\mathrm{MPa}$ is applied to the crystal, the hysteresis responses change significantly, as shown in figure 1.6(c) and (d) [28]. The applied stress induces 90° switching in the crystal which drives the variants with out-of-plane polarization to switch into the in-plane variants when the electric field is around zero. As the electric field increases, another 90° switching occurs. The in-plane variants switch to the crystal variant with polarization direction parallel to the applied electric field, and a state of saturation is then reached. This two-step 90° switching results in kinks (points K) at the two steep portions of the dielectric loop shown in figure 1.6(c), and gives a large butterfly-shape hysteresis with significant straining in figure 1.6(d). The hysteresis loop of a ferroelectric crystal varies in size and shape according to its material composition, microstructure and applied boundary conditions. It is a good way of identifying and characterizing a ferroelectric material [23].

1.3 Background: micromechanical switching models

As the poling process and hysteresis response are important in respect of macroscopic behaviour of ferroelectrics, many models of ferroelectric switching have been developed in recent decades. A key feature in micromechanical switching models is that the ferroelectric crystal is treated as a material containing regions with different polarized states [29]. The model developed by Hwang *et al.* [30] is an example of micromechanical modelling, wherein a polycrystal is represented by many randomly oriented single crystal grains. Uniform stress is assumed throughout the entire polycrystal, and each grain contains just one crystal variant. The central idea of this model is that switching occurs when the work done by local electro-mechanical fields exceed a critical threshold. Similar concepts are used and extended in many other models [31–33]. A natural extension is to model grains containing multiple domains, and allow incremental switching of material between domain types [34]. This can provide a smoother and more accurate prediction of hysteresis response [29]. In polycrystal models, various methods have been employed to account for the inhomogeneity of stress and electric fields. At the simplest level, the Reuss approximation of uniform stress and electric field [30–32] neglects inhomogeneity, while self-consistent theory [34–36] estimates the interaction between grains and their surroundings using the Eshelby inclusion method. Finite element studies [37–41] allow detailed computation of the fields in each grain at the cost of computational resources.

Models of polycrystals commonly exploit the randomness of the microstructure to smear out the material response. By contrast, single crystals show ordered patterns of domains that affect the overall behaviour. By "domain engineering" stable domain structures can be formed that enhance the electromechanical properties and performance [4, 5, 26, 42–45]. Domain structure in single crystals also strongly influences the ferroelectric hysteresis, coercive field and remanent polarization [7, 28, 46–49]. Thus modelling of both the small field and large field properties of single crystals should take into account the domain structures that form in the crystal.

1.4 Background: laminate theory of ferroelectric domains

In ferroelectric applications, organized or "engineered" ferroelectric domains give properties such as piezoelectricity and remanent polarization. External load can rearrange the domain pattern giving effects such as ferroelectric switching. Processes, such as poling, rely on the ability of the microstructure to evolve under external loads. Consequently, microstructure plays a key role in varying material properties for device design. To have better understanding of ferroelectric microstructures, several models predicting the equilibrium structure of ferroelectric crystals and related systems have been studied which are based on energy minimisation [24,50]. Central to these studies is the idea that domain pairs adopt orientations that eliminate internal charge and misfit strain at their common interface.

By using the principles of domain wall compatibility [24], an elegant model of domain structure was proposed by Li and Liu [26] following Bhattacharya [51] and DeSimone and James [52]. Their approach models the microstructure as a periodic, multi-rank laminate of ferroelectric domains in which compatibility requirements are satisfied at each level of lamination, giving a low energy structure overall. Figure 1.7 shows schematic rank-1, rank-2, and rank-3 laminate domain structures. The model of Li and Liu enables the construction of a laminate corresponding to any given state of average strain and polarization within the limits imposed by saturation of volume fractions. It also allows an exact determination of the effective material coefficients, such as the elastic and piezoelectric properties in such a laminate. However, when pairs of laminates are conjoined to form a higher-rank lamination in the model of Li and Liu, the compatibility conditions are satisfied only in a volume average sense, which can result in local incompatibilities between sub-laminates. The term "compatible on average" (COA) is used in this thesis to describe such structures. Clearly structures of this kind may not be minimum energy structures because of the energy associated with local incompatibilities.

This local incompatibilities issue is largely resolved by the concept of a fine phase mixture [50] and a separation of length scales, wherein the sub-laminations are taken to be suffi-

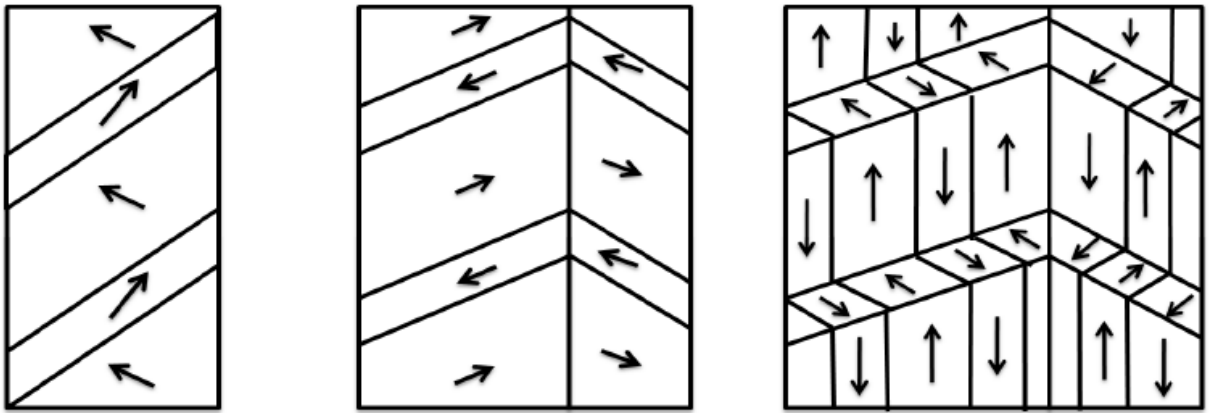

Figure 1.7: Schematic illustrations for periodic (a) rank-1, (b) rank-2, and (c) rank-3 laminate structures.

ciently fine that the resulting laminate can be treated as a homogeneous medium, as shown in figure 1.8. However, in a multi-rank laminate, separation of length scales between successive laminations generally results in extremely fine microstructure at the lowest level of lamination. The energy associated with the domain walls themselves, which is commonly neglected, may then become significant. Thus it appears likely that, among compatible laminate structures, those of lower rank are energetically favourable. Direct observation of real microstructures commonly reveals local regions of low-rank lamination; for examples of such structures see figure 1.3 or figure 1.9. Real microstructures are typically inhomogeneous, containing multiple regions of low-rank compatible laminate structure, with differing length scales and arrangement. The opportunity to engineer low energy configurations offers some potential advantages, such as the possibility of poling routes that minimise stresses during the poling operation. This motivates the current study of compatible multi-rank laminates, with a view to finding the minimum rank solutions to the compatibility equations. In the current work, the compatibility of a wide range of laminated structures is considered. The study is limited to periodic laminate structures only, with the aim of identifying possible structural arrangements that may be of interest from the point of view of designing or engineering domain structure.

As mentioned in section 1.2, multiple solutions for a low energy domain wall orientation result in the domain configuration of minimum energy being non-unique. The complexity caused by this non-uniqueness is partly resolved within the scheme of Li and Liu [26] by

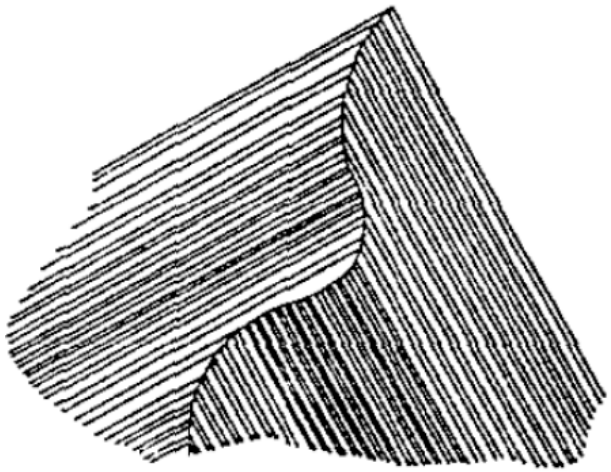

Figure 1.8: A schematic illustration of fine phase mixture with a separation of length scales. The resulting laminate can be treated as a homogeneous medium [50].

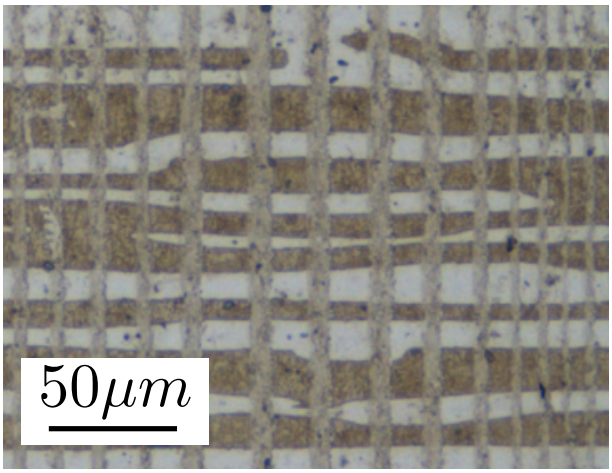

Figure 1.9: Direct observation of the low-rank lamination.

restricting the composition of laminations such that the layers always share common crystal variants. The cost of this simplification is that, in general, a laminate structure of the Li-Liu type containing n crystal variants has rank $n - 1$ (this will be discussed in detail in chapter 2). For example, the tetragonal crystal with six variants produces very complex rank-5 laminates. It is often possible to find simpler structures, which are multi-rank laminates with rank less than that generated by Li and Liu's procedure.

In addition to considering compatibility on average, further complications arise if an "exactly compatible" (EC) microstructure is sought. This term will be used for laminate microstruc-

ture in which every domain wall satisfies the compatibility equations which will be described in detail in chapter 2. An EC laminate must satisfy the conditions for COA laminates, but more than that, sub-laminations must have equal domain wall spacing and orientation at their common interfaces. This strongly constrains the possible pairings of neighbouring domains in multi-rank EC laminates because a high rank interface in the laminate may form a domain wall between several distinct pairs of crystal variants. It is reasonable to expect that EC structures have low energy by comparison with COA structures of similar rank. This motivates the present work, where a systematic study of COA and EC structures is made, with a view to finding minimum rank EC microstructures.

The effect of a finite lattice shear strain between distinct crystal variants should also be considered. In barium titanate, for example, the tetragonality of the unit cell is close to 1%. This causes the true lattice rotation at a 90° domain wall to be 90.62° [24]. The schematic illustration can be seen in figure 1.4(b). Thus lattice planes turn by 0.62° across the domain wall, and this can contribute 0.62° of disclination at a junction of 90° domain walls [3]. Where groups of domains meet, the requirement for continuity of the crystal lattice imposes a compatibility constraint relating to the disclinations. This issue has been studied in groups of four domains (quadruplets) meeting at a line by Fousek and Mokry [53], who use the term "clapping angle" to describe the total disclination at the junction of a quadruplet. Either the disclination vanishes, to give a stress-free compatible arrangement, or continuity is preserved by a state of stress at the domain junction. Savytskii and Bismayer [54] consider the strain at multi-domain junctions and illustrate some compatible arrangements in trigonal, orthorhombic and monoclinic crystals. Thus, compatible domain arrangements of low rank with vanishing total disclination at every junction, i.e. disclination free (DF) arrangements, are also of interest and discussed in the present work.

1.5 Background: domain evolution models

In ferroelectrics, the domain pattern greatly influences the switching behaviour, motion of domain walls and electromechanical hysteresis response. Models which take domain structure into account fall broadly into two types, diffuse interface and sharp interface, depending on how the domain wall is represented. Diffuse interface models treat the domain walls as part of a continuum with the polarization varying continuously through the wall. Among diffuse interface approaches, the phase field method is one of the most commonly used techniques. Atomistic calculations such as *ab initio* models also have great potential to model equilibrium domain structures [55–57]. By contrast, in sharp interface models there is a jump in polarization at the domain wall, and the detailed structure of the wall is neglected. Here, several phase field and sharp interface models are discussed and compared.

1.5.1 Phase field models

A phase field model describes ferroelectric domain patterns by using an order parameter that takes on distinct values in the different domains [6]. Various choices of order parameter are possible, but the chosen parameter must be able to discriminate among the set of crystal variants. For example, the local polarization is a convenient choice of order parameter, as it usually takes on a distinct value in each crystal variant. Then a region with uniform polarization has uniform order parameter, representing a single domain, and the transition region between a pair of domains has a continuously varying order parameter, indicating a domain wall. A major advantage of this method is that it requires no prior assumptions of domain structures which might form [8]. However, phase field models [6–22] must resolve the domain wall, which is commonly of order nanometres in thickness [58]. Thus, where discretization is used, many elements are needed to simulate regions of microstructural scale.

The evolution of domain structure from a non-equilibrium state towards an equilibrium state reduces the free energy, consisting of the bulk free energy, domain wall energy, electrostatic and elastic energy, and the potential energy of applied loads. These energies can be expressed in terms of the chosen order parameter. For example, in a typical phase field model [8], the spontaneous polarization $\mathbf{P}(\mathbf{r}, t)$ is chosen as the order parameter, where $\mathbf{r}$ is the position vector and t is time. The total free energy in the crystal with volume V is given by

$$F = \int_V (f_{bulk} + f_{elas} + f_{grad} + f_{elec}) \mathrm{d}V \tag{1.3}$$

where f_{bulk}, f_{elas}, f_{grad}, and f_{elec} are the bulk free energy density, the elastic energy density, the gradient energy density, and the electrostatic energy density, respectively. The bulk free energy density f_{bulk} is typically set as a function of polarization, producing a multi-well structure that can describe different phases. The f_{bulk} term has a local minimum whenever the polarization aligns to a crystal variant. The elastic energy density f_{elas} is a function of the elastic strain, which is the difference between the total strain of the crystal and the spontaneous strain; this is assumed to be quadratically related to the polarization. Minimisation of f_{elas} thus drives material towards the spontaneous strain state corresponding to the current polarization. The domain wall energy arises from the gradient energy density f_{grad}. It is commonly assumed to be proportional to the square of the magnitude of polarization gradient, which is nonzero only near domain walls. Finally, the electrostatic energy density f_{elec} accounts for dipole interactions, depolarization fields due to surfaces, and the applied electric field.

The minimisation of free energy can be achieved by a relaxation method, with linear kinetics. This leads to an evolution law in the form of the time-dependent Ginzburg-Landau (TDGL) equation [59, 60]:

$$\frac{\partial \mathbf{P}(\mathbf{r}, t)}{\partial t} = -L \frac{\partial F}{\partial \mathbf{P}(\mathbf{r}, t)} \tag{1.4}$$

where L is a kinetic coefficient related to the mobility of domain walls. By solving equa-

tion (1.4) the details of the evolution under the given loads can be determined and equilibrium states of the order parameter can also be found. Figure 1.10 shows examples of 2 and 3-dimensional structures under electromechanical loads that were predicted by a typical phase field model developed by Choudhury *et al.* [8].

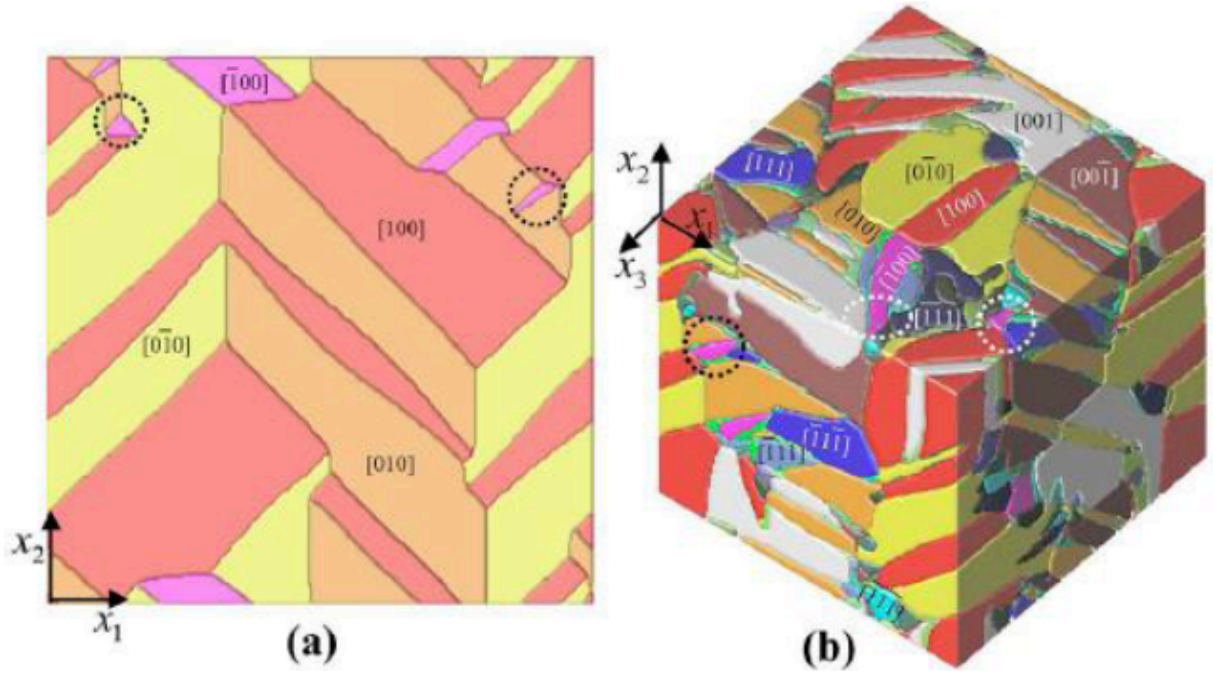

Figure 1.10: Domain structures of a ferroelectric single crystal obtained from the phase field model by Choudhury *et al.* [8]. The polarization directions of the distinct phases and domain types are shown in different colours. (a) Domain structure from the 2D simulation; (b) Domain structure from the 3D simulation.

Models using this theory usually choose the polarization as the primary order parameter, with most adopting periodic boundary conditions for the convenience of computation. These models have been applied to study a wide variety of problems related to ferroelectric microstructure. Cao and Cross [16] studied the twin structure and domain wall orientation in the tetragonal crystal system. Hu and Chen [11] have successfully modelled the transformation between cubic and tetragonal phases in bulk barium titanate. Wang *et al.* [17] reveal the evolution of domain structure during switching under electromechanical loads. Zhang and Bhattacharya [18, 19] solve explicitly for the electrostatic potential and thereby study non-periodic domain structure.

More recently, Choudhury *et al.* [8] studied the relationship between the value of the coercive field and the presence of different types of domain in bulk ferroelectric crystals. Su and Landis [7] investigated the electromechanical pinning effect of charges on 180° and 90° domain walls. Using the same model, Kontsos and Landis [20, 21] further investigated pinning by dislocations, and the formation of domain structure in thin films.

The main differences between phase field models are in the treatment of various contributions to the total energy expression [6] and the choice of order parameter. Choices of order parameter other than the local polarization have also yielded valuable insights. Shu *et al.* [13] introduce the concept of hierarchical laminate structures into their model and include the volume fractions of laminates as order parameters in addition to polarization. The resulting "non-conventional" phase field model makes the well structure of the free energy more explicit, reducing the number of fitting parameters required. The method has been used to study stable periodic domain patterns [22].

1.5.2 Sharp interface models

Sharp interface approaches [61–64] treat a domain wall as a discontinuity, across which the polarization and strain may jump. Thus, a significant saving of computation can be achieved compared to diffuse interface models, and the study of large 3-dimensional regions then becomes feasible. A common approach is to treat the domain wall as a crystal defect and find the driving force for motion of that defect, for example through the use of the Eshelby energy momentum tensor [61, 65, 66]. Motion of domain walls can be predicted, and equilibrium domain arrangements obtained. It is often convenient to assume particular domain topologies in models of this type. If flat domain walls are assumed, simple evolution laws can be found [62, 63]. When considering periodic structure, it can be convenient to treat the volume fractions of the crystal variants as thermodynamic variables [62, 64, 67]. Alternatively, the positions of individual domain walls [63] or length of a growing feature [61] may be used as the variables. The use

of the Eshelby energy momentum tensor requires knowledge of local fields that can be derived by solving for the equilibrium of the system in its current configuration. Alternatively, a global approach may be used, in which a global potential is minimised. In either case a kinetic relation is needed to infer the rate of domain wall motion from the driving force. Linear kinetics are commonly assumed, and this introduces the domain wall mobility as a factor governing the rate of domain wall motion.

Loge and Suo [61] introduced a variational principle that forms the basis for the global approach and formulated a kinetic model using a functional in the form of:

$$\Pi = \dot{G} + \Psi \tag{1.5}$$

where G is the Gibbs free energy which is the sum of the internal stored energy and potential energy due to the loads, and Ψ is a dissipation rate potential associated with the area, velocity, and mobility of domain walls. It is readily shown that the domain structure evolves along a path which makes the functional Π stationary [61, 68] with respect to the domain wall velocity $v_{(W)}$, that is:

$$\frac{\partial \Psi}{\partial v_{(W)}} = -\frac{\partial \dot{G}}{\partial v_{(W)}} \tag{1.6}$$

The domain wall velocities $v_{(W)}$ can be obtained directly by solving equation (1.6); the path of domain evolution can then be found. In the work of Loge and Suo [61], the evolution of a one degree of freedom domain stripe and an elliptical domain region with two degrees of freedom were studied. Similarly, Huber and Cocks [63] use the variational principle, previously applied to a variety of problems in microstructure evolution [68], to model the hysteresis response of $BaTiO_3$. In their model, a domain pattern with two degrees of freedom and linear kinetics were assumed. Yen *et al.* [64] combine the concept of a switching criterion and compatible laminate theories [26] to model the hysteresis response of $BaTiO_3$, assuming a multi-rank averagely-compatible laminate structure. Similar work by Weng and Wong [62] develops a ther-

modynamic framework for specific rank-1 and rank-2 compatible domain laminates, such as the commonly observed herringbone pattern [1]. Their model predicts the hysteresis response of $BaTiO_3$, showing features in common with the results of experiments by Burcsu *et al.* [28].

Many sharp interface models have been used to predict the hysteresis response corresponding to particular domain patterns, such as polarization vortices [63, 69] and herringbone domains [48, 62]. However, most of these models do not allow the possibility of new domain patterns nucleating. It is worth noting that when simulating the electromechanical behaviour by sharp interface approaches, the resulting hysteresis response is largely dependent on the choices of domain patterns made by researchers. Therefore, a sharp interface model within which new domain patterns may nucleate when they become energetically favourable, is still desirable. This motivates the current study, where we introduce the new concept of transitional "pivot states" which allows the switching between distinct domain patterns and eliminates the assumption of one particular microstructure in the crystal. This may be of technological interest from the point of view of designing or engineering domain structures.

1.6 Background: models for ferroelectric films

The models discussed so far focus on bulk ferroelectric crystals; however, thin film devices have also been studied extensively in the last decade. Ferroelectric films have many advantages in applications, such as small size, low operating voltage, high speed, and ease of production for materials that are difficult to produce in bulk [23]. Furthermore, ferroelectric films have great potential for domain engineering, for example by rearranging the domain orientation using techniques such as conductive atomic force microscopy [70]. This can create new structures with attractive properties [71]. Alternatively, periodic structures in films can be used to provide a template for a patterned device [72].

In ferroelectric films, both the crystallographic orientation and the strain state of the film are strongly influenced by the substrate. This dramatically affects the properties of the film, such as Curie temperature and microstructure [73]. For example, when a $BaTiO_3$ film is subjected to a biaxial compressive substrate strain, its cubic-to-tetragonal transition temperature can be increased by as much as $500\ ^\circ\mathrm{C}$ relative to a bulk single crystal [74]. The substrate constraint also imposes a state of in-plane strain that governs the stable domain structure. In sufficiently thin films, the compatibility constraints are relaxed in the out-of-plane direction as the deformation energy becomes much smaller than the interfacial and membrane energies [75]. Thus, a low energy elastic accommodation to out-of-plane incompatibilities is possible. As a consequence, thin films can allow a greater range of low energy domain structures than bulk crystals.

In recent years, researchers have explored the switching behaviour, microstructural thermodynamics, phase diagrams, and effects of misfit strain in ferroelectric thin films [71, 73, 76–84]. Speck and Pompe [79] calculated the microstress due to the misfit strain and its effect on the energy of epitaxially grown films. They used temperature dependent stability maps to illustrate the behaviour of domain structures in thin films. Roytburd *et al.* [71, 77] developed a thermodynamic theory based on theories of elastic domains to study the influence of the misfit of strains on the domain structure. Based on this theory, Alpay *et al.* [78] produced domain stability maps for tetragonal ferroelectric thin films. The effect of a uniaxial external stress on the domain stability maps was discussed. The related topic of martensitic transformations in constrained thin films was also studied by Roytburd *et al.* [85]. They represented the domain structure as a multi-rank laminate of different types of domain in order to calculate the overall strain states and the evolution of domain patterns. Pertsev *et al.* [80] adopt the thermodynamic calculations to give several domain stability maps for $BaTiO_3$ and $PbTiO_3$.

Prior thermodynamic analyses in ferroelectric films generally focused on the tetragonal crystal system and simplified the six types of domain orientations into three, i.e. domains with parallel polarization directions were treated as identical. Then, the two types of domain with

their polarization orientations parallel to the substrate surface are named a_1 and a_2 domains, while c domains contain the variant with polarization perpendicular to the film surface. Moreover, certain particular domain structures are commonly assumed, such as alternating $c/a/c/a$ or $a_1/a_2/a_1/a_2$ domain patterns [76, 80]. However, under certain boundary conditions, these patterns may not form, as a domain arrangement with other types of domain present is energetically favourable [86]. Li *et al.* [73, 81, 83] used a phase field model of domain evolution in 3-dimensions without any prior assumptions of domain pattern. All three types (a_1, a_2, c) of tetragonal domain were found to co-exist and complicated structures resulted.

Several different approaches have also been used to study the switching behaviour and domain structure in ferroelectric or other related crystalline films. Huber [82] adapts a self-consistent micromechanics model with some modifications to satisfy thin film conditions for prediction of the hysteresis response of a lead zirconate titanate (PZT) film. Similar methods were used by Pane *et al.* [87,88] to study the effects of film geometry and mechanical constraint on dielectric hysteresis. In the study of martensitic trigonal thin films, Shu and Yen [84] employ the "non-conventional" phase field approach to investigate the formation of low energy domain patterns.

1.7 Layout of this thesis

Chapter 2 starts with an introduction to the theory of domain compatibility. A binary tree representation is used to define hierarchical multi-rank laminate structures; the conditions for compatibility on average (COA), exact compatibility (EC), and disclination-free compatibility (DF) are stated in relation to the binary tree. In addition, a geometric analogy between a rank-R laminate and the cube in R-dimensions is introduced to represent the relationship of orientation between domain pairs.

In chapter 3, a systematic search is applied to find minimum rank compatible structures in the tetragonal and rhombohedral crystal systems. Minimum rank laminate structure is discussed and low rank poling paths in average strain and polarization space are found. The existence of low rank, exactly compatible poling paths in the tetragonal and rhombohedral crystal systems is demonstrated. Furthermore, the method is applied to classify and enumerate rank-2 laminate domain patterns that can form in the polar tetragonal and rhombohedral crystal system. Surprisingly, a very limited number of distinct EC rank-2 laminate patterns are found to exist. These patterns are classified and correlated with observations of domains in single crystals.

In chapter 4, the compatibility conditions mentioned in chapter 2 are modified and applied to ferroelectric films. Exactly compatible laminate structures in $[001]$, $[011]$, and $[111]$ oriented rhombohedral and tetragonal films are discovered and studied. The results indicate several poling paths along which the microstructure can evolve continuously while maintaining compatibility. The poling ability, or limit on the maximum polarization achieved is discussed. The influence of a strain state imposed by the substrate on the microstructure and the effect on poling ability is studied.

Chapter 5 presents a variational method, which minimises a functional associated with free energy and dissipation potential. The dynamic behaviour of periodic compatible laminate domain patterns in the tetragonal crystal system, such as microstructure evolution and hysteresis response, are studied. Then, the concept of transitional "pivot states" is introduced. This allows the crystal with one type of domain pattern to switch to another pattern. The possibility of nucleation of new domain patterns is then incorporated into the variational model. This is applied to study the hysteresis responses of barium titanate ($BaTiO_3$) single crystals subjected to variety of loads.

Chapter 6 presents a discussion of the contents of the thesis and conclusions of the research. It also suggests improvements of the current approaches and outlines the future research.

2

Theory of compatibility

2.1 Energy minimisation and single domain states

A ferroelectric crystal can adopt a minimum energy equilibrium state by arrangement of its domain microstructure. Shu and Bhattacharya [24] described the energy minimisation problem in a ferroelectric region $\Omega \in \mathbf{R}^3$ with boundary $\partial\Omega$ carrying tractions $\mathbf{T}_0$ and with surface conductors carrying charge Q at electrical potential ϕ^0, as shown in figure 2.1. The total energy is then:

$$F(\mathbf{u},\mathbf{p}) = \int_\Omega (\frac{1}{2}\nabla\mathbf{p}\cdot\mathbf{A}\nabla\mathbf{p} + W(\boldsymbol{\epsilon},\mathbf{p}) - \mathbf{E}_0\cdot\mathbf{p})\mathrm{d}\mathbf{x} - \int_{\partial\Omega}\mathbf{T}_0\cdot\mathbf{u}\mathrm{d}s + \frac{\epsilon_0}{2}\int_{\mathbf{R}^3}|\nabla\phi|^2\mathrm{d}\mathbf{x} \quad (2.1)$$

where $\mathbf{u}$ and $\mathbf{p}$ are the displacement and polarization, $\mathbf{A}$ is a constant positive definite matrix, $\boldsymbol{\epsilon}$ is the strain tensor, $\mathbf{E}_0$ is the electric field in the absence of the ferroelectric, ϵ_0 is permittivity of free space, and ϕ is the electric potential. The first term of equation (2.1) represents domain wall energy; the quadratic dependence on $\nabla\mathbf{p}$ penalizes gradients of polarization, and that makes uniform polarized domains preferable. The second term, W, is the internal energy and has a well structure to produce one of a set of stable combinations of strain and polarization corresponding to known domain states. The third term is the potential energy due to the application of electric field $\mathbf{E}_0$; this term aligns the polarization of the crystal with $\mathbf{E}_0$. The fourth and fifth terms are

the potential energy of the tractions $\mathbf{T}_0$ and the depolarization energy due to the permittivity of free space.

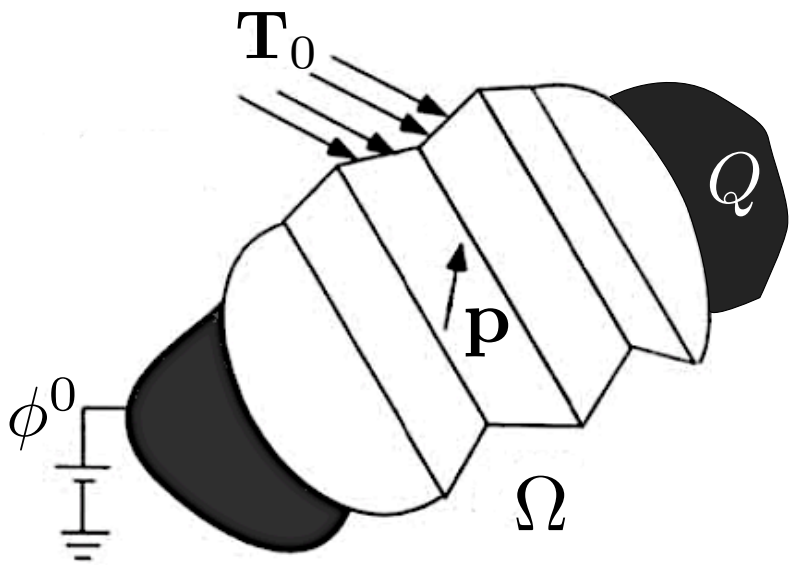

Figure 2.1: A ferroelectric system Ω under tractions $\mathbf{T}_0$, and with surface conductors carrying charge Q at electrical potential ϕ^0. (modified from Shu and Bhattacharya [24])

A stable equilibrium structure minimises the functional F with respect to variations in the fields $\mathbf{u}$ and $\mathbf{p}$. In the constrained theory of domains [26,52], the functional F is minimised subject to the pointwise constraint that $W(\boldsymbol{\epsilon}, \mathbf{p}) = 0$. Then each point has a strain and polarization state taken from the set of energy wells in W and domain walls are treated as sharp interfaces. Under the assumption that the size of a domain is much larger than the domain wall thickness, the first term in equation (2.1) can be neglected. Equation (2.1) has the effect of selecting domain states that are energetically favoured by the external loads and boundary conditions. For certain combinations of external loading and boundary conditions, this results in a single crystal variant throughout Ω. Then the body assumes a single domain state and its properties are identical to those of a pure crystal variant. However, when the boundary conditions are not consistent with a single domain state, the minimum energy configuration consists of more than one domain. This raises the problem of arranging multiple domains so as to minimise energy.

2.2 Compatibility of a domain pair

When the loads and boundary conditions favour the coexistence of two variants in the crystal, the total energy $F(\mathbf{u}, \mathbf{p})$ is minimised by a domain configuration that satisfies compatibility conditions. Consider a crystal that has undergone transformation to the ferroelectric phase. Assume that the crystal turns into the state shown in figure 2.2, containing two regions Ω_i, Ω_j separated by a interface with unit normal vector $\mathbf{n}$. Two crystal variants i, j with spontaneous polarization $\mathbf{p}_i$, $\mathbf{p}_j$ are induced; regions Ω_i, Ω_j are subjected to distinct strains; yet note that the crystal remains continuous. The deformation $\mathbf{y}(\mathbf{x})$ is piecewise homogeneous, and the deformation gradient $\nabla\mathbf{y}$ of regions Ω_i, Ω_j are $\mathbf{G}_i$ and $\mathbf{G}_j$, respectively [89]. Since the deformation is continuous across the common interface between regions, it is necessary that $\mathbf{G}_i$ and $\mathbf{G}_j$ satisfy the "Hadamard jump condition" [90]

$$\mathbf{G}_i - \mathbf{G}_j = \mathbf{a} \otimes \mathbf{n} \tag{2.2}$$

where $\mathbf{a}$ is an arbitrary vector. To see this, we can consider that the deformations along any

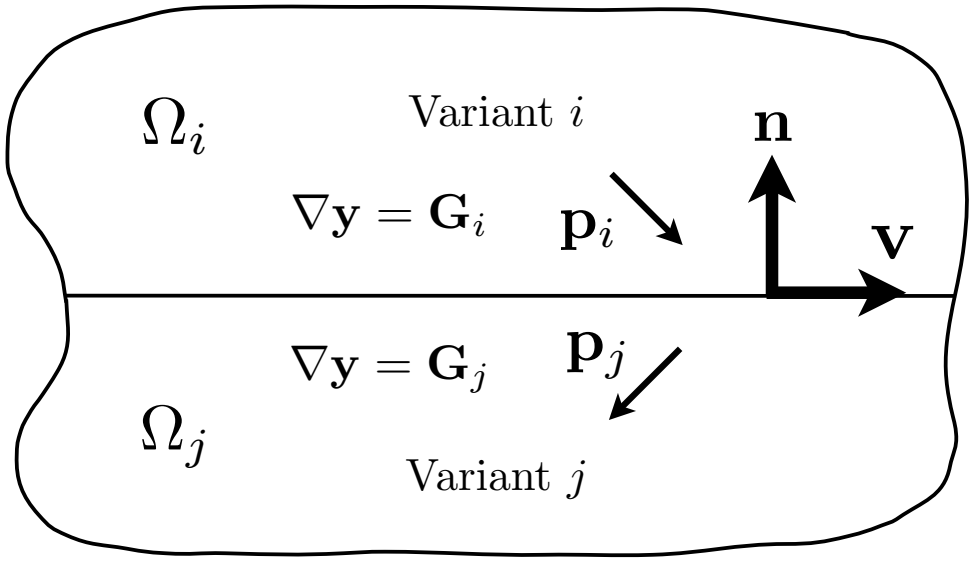

Figure 2.2: A crystal contains regions Ω_i and Ω_j with two ferroelectric crystal variant i and j. (modified from Bhattacharya [89])

direction vector $\mathbf{v}$ lying on the interface from both sides are required to be identical, that is

$$\mathbf{G}_i\mathbf{v} = \mathbf{G}_j\mathbf{v} \tag{2.3}$$

Note that vector $\mathbf{v}$ is perpendicular to $\mathbf{n}$ which implies $\mathbf{n}\cdot\mathbf{v} = 0$, and equation (2.3) can be rearranged as

$$(\mathbf{G}_i - \mathbf{G}_j)\mathbf{v} = \mathbf{0} = (\mathbf{n}\cdot\mathbf{v})\mathbf{a} = (\mathbf{a}\otimes\mathbf{n})\mathbf{v} \tag{2.4}$$

The Hadamard jump condition is then obtained. However, when considering infinitesimal strain for engineering purposes, we can approximate the strain matrix as $\boldsymbol{\epsilon} = \frac{1}{2}(\mathbf{H} + \mathbf{H}^T)$, where $\mathbf{H}$ is displacement gradient, i.e. $\nabla\mathbf{u}$. We can use the relationship between deformation gradient and displacement gradient to rewrite $\mathbf{G}_i$ and $\mathbf{G}_j$

$$\mathbf{G}_i = \mathbf{H}_i + \mathbf{I}\,, \qquad \mathbf{G}_j = \mathbf{H}_j + \mathbf{I} \tag{2.5}$$

where $\mathbf{I}$ is an identity matrix. According to equations (2.2) and (2.5), we can obtain

$$\boldsymbol{\epsilon}_i - \boldsymbol{\epsilon}_j = \frac{1}{2}(\mathbf{a}\otimes\mathbf{n} + \mathbf{n}\otimes\mathbf{a}) \tag{2.6}$$

This is the well-known linearised kinematic strain compatibility equation, and is extensively used in the theory of martensite, as well as ferroelectric studies. Domain structures which satisfy this condition minimise the elastic energy term in equation (2.1).

In addition to the elastic energy, the stored dielectric energy also needs to be minimised. This requires that there is no net charge on the boundary between domains, i.e. the polarization field is divergence free, $\nabla\cdot\mathbf{p} = 0$. This condition implies $\mathbf{p}_i\cdot\mathbf{n} = \mathbf{p}_j\cdot\mathbf{n}$, and can be rearranged in the form of

$$(\mathbf{p}_i - \mathbf{p}_j)\cdot\mathbf{n} = 0 \tag{2.7}$$

Thus, for domain pair i and j with strain states $\boldsymbol{\epsilon}_i$, $\boldsymbol{\epsilon}_j$ corresponding polarization vectors $\mathbf{p}_i$, $\mathbf{p}_j$,

the interface normal vector $\mathbf{n}$ of a compatible domain wall must satisfy compatibility equations (2.6) and (2.7) to form a low energy domain structure [26, 50, 52].

In the present work, consideration is limited to sets of crystal variants which are mutually related by pure rotations. This is typical of ferroelectric crystals. Thus the lattice strains can be represented with respect to a reference state by strain tensors $\boldsymbol{\epsilon}_i$ that are trace-free, and the unit cells of each crystal variant have identical volume. Strain compatibility equation (2.6) can then be solved by using the eigenvalues λ_k and eigenvectors $\mathbf{e}_k$ $(k = 1 \ldots 3)$ of the matrix $\mathbf{M} = \boldsymbol{\epsilon}_i - \boldsymbol{\epsilon}_j$. Because of the condition of trace-free strain $\boldsymbol{\epsilon}_i$ at least one eigenvalue of $\mathbf{M}$ is zero. Let $\lambda_3 = 0$; then two solutions for the interface normal $\mathbf{n}$ are given by

$$\mathbf{n} = \frac{\pm\sqrt{-\lambda_1/\lambda_2}\mathbf{e}_1 + \mathbf{e}_2}{\sqrt{1 - \lambda_1/\lambda_2}} = \frac{\mathbf{e}_2 \pm \mathbf{e}_1}{\sqrt{2}} \tag{2.8}$$

The resulting vector $\mathbf{n}$ may be substituted into equation (2.7) to check polarization compatibility. Figure 2.3 shows three examples of compatible and incompatible domains in the tetragonal crystal system. In this crystal system, there are six crystal variants in three oppositely polarized pairs with polarization vectors $\mathbf{p}_{(k)}$ $(k = 1 \ldots 6)$ directed along three orthogonal axes. Each polarization state has a corresponding strain state

$$\boldsymbol{\epsilon} = \alpha^t \mathbf{I} + (\beta^t - \alpha^t)\hat{\mathbf{p}} \otimes \hat{\mathbf{p}} \tag{2.9}$$

where α^t and β^t are material parameters, $\hat{\mathbf{p}}$ is the unit vector in the polarization direction, and $\mathbf{I}$ is a 3×3 identity matrix. Figure 2.3(a) shows a pair of variants with anti-parallel polarization states, $\mathbf{p}_1 = -\mathbf{p}_2$. Their strain states are identical ($\mathbf{M} = \boldsymbol{\epsilon}_i - \boldsymbol{\epsilon}_j = \mathbf{0}$) and thus equation (2.6) is trivially satisfied for any $\mathbf{n}$ by setting $\mathbf{a} = \mathbf{0}$. However, the structure shown gives "head to head" polarization vectors which violate equation (2.7). To form a compatible structure for this anti-parallel domain pair, the interface normal must be perpendicular to the polarization difference $\mathbf{p}_i - \mathbf{p}_j$. This would give a continuous set of solutions for $\mathbf{n}$ and results in domain walls

without a unique habit plane. A second incompatible structure is shown in figure 2.3(b). It contains two tetragonal crystal variants with perpendicular polarizations, in the $[1, 0, 0]$ and $[0, 0, 1]$ directions. The interface normal vector $[0, 1, 0]$ satisfies equation (2.7) but not equation (2.6). The unique compatible habit plane of this $90°$ domain pair has normal vector $[1, 0, 1]$ as shown in figure 2.3(c). In this structure, strain and polarization compatibility are both satisfied giving a commonly occurring "head to tail" polarization pattern.

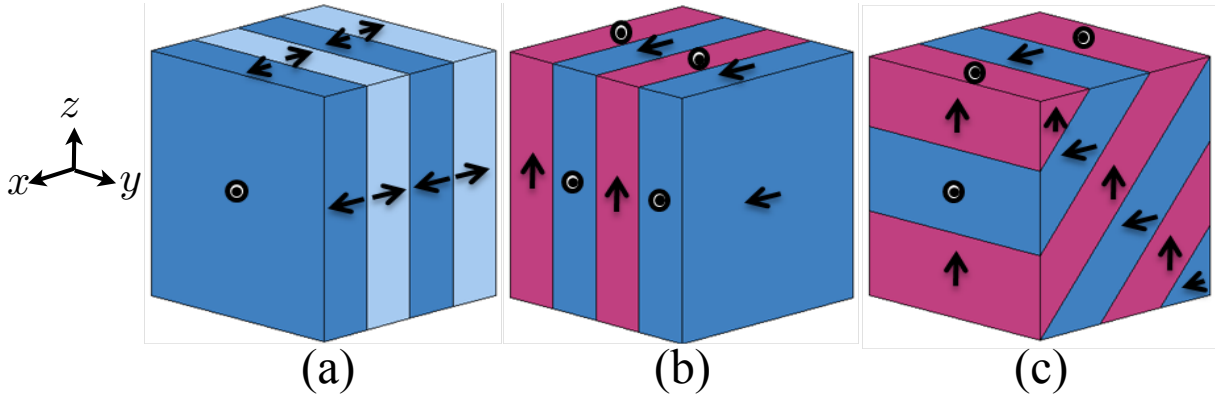

Figure 2.3: Tetragonal crystals which are (a) compatible in strain but not polarization, (b) compatible in polarization, but not strain, and (c) compatible in both polarization and strain.

It is worth noting that any single crystal variant can form a compatible interface with any other single variant in the same crystal system if the crystal variants are related by a pure rotation. One can always predict the orientation of the domain interface for any domain pair by solving the compatibility equations (2.6) and (2.7). Thus, for a pair of tetragonal crystal variants, the domain configuration is either unique or allows a continuous set of solutions for $180°$ domain pairs. A simple EC structure in the form of a rank-1 laminate can always be formed. However, groups of more than two crystal variants may require a higher rank laminate structure; thus more compatibility conditions are provided for domain configuration in the following sections.

2.3 Compatibility of laminate structures

2.3.1 Binary tree diagram and crystal variant arrangement

In laminated domain structure, pure variants can be regarded as rank-0 laminations, while a pair of variants can be laminated to form a rank-1 lamination. Similarly, pairs of laminates can themselves be laminated to form a higher rank lamination. Thus, a hierarchical binary tree diagram can be introduced to represent the arrangement of domains in a rank-R laminate. The same representation is used by Goldsztein [91]. For example, figure 2.4 shows the tree diagram representing a rank-2 lamination. A top-down numbering of the nodes is used. The first node (root node), at the top level of the tree, represents the entire laminate. Nodes at lower levels in the tree represent structures that are conjoined to form higher rank laminations. At the lowest level, the nodes represent pure crystal variants. The tree diagram of a rank-R domain configuration contains $2^{R+1} - 1$ nodes and $R + 1$ levels. Relationships between nodes can be found by examining their node numbers: for example parent node i consists of child nodes $2i$ and $2i + 1$. These relationships make the tree diagram a convenient representation of laminated domain structure for computational purposes. For clarity, we introduce a simple way to distinguish and label laminate structures, using the variant numbers in the lowest level of the tree diagram. For example, the rank-2 laminate in figure 2.4 is labeled 1234, while the rank-1 laminate represented by node 2 is labeled 12, and similarly the laminate at node 3 is labeled 34.

In general, each node represents a material characterized by two properties: an average strain, and an average polarization. Apart from nodes in the lowest level, all nodes are associated with an interface normal vector $\mathbf{n}_i$ that specifies the orientation of the lamination and a domain wall spacing l_i which describes the physical size of the layers. Changing the domain wall spacings can make a significant difference to the appearance of a laminate without altering its topology. For example, figure 2.5(a) is the domain structure 1234 with domain spacing

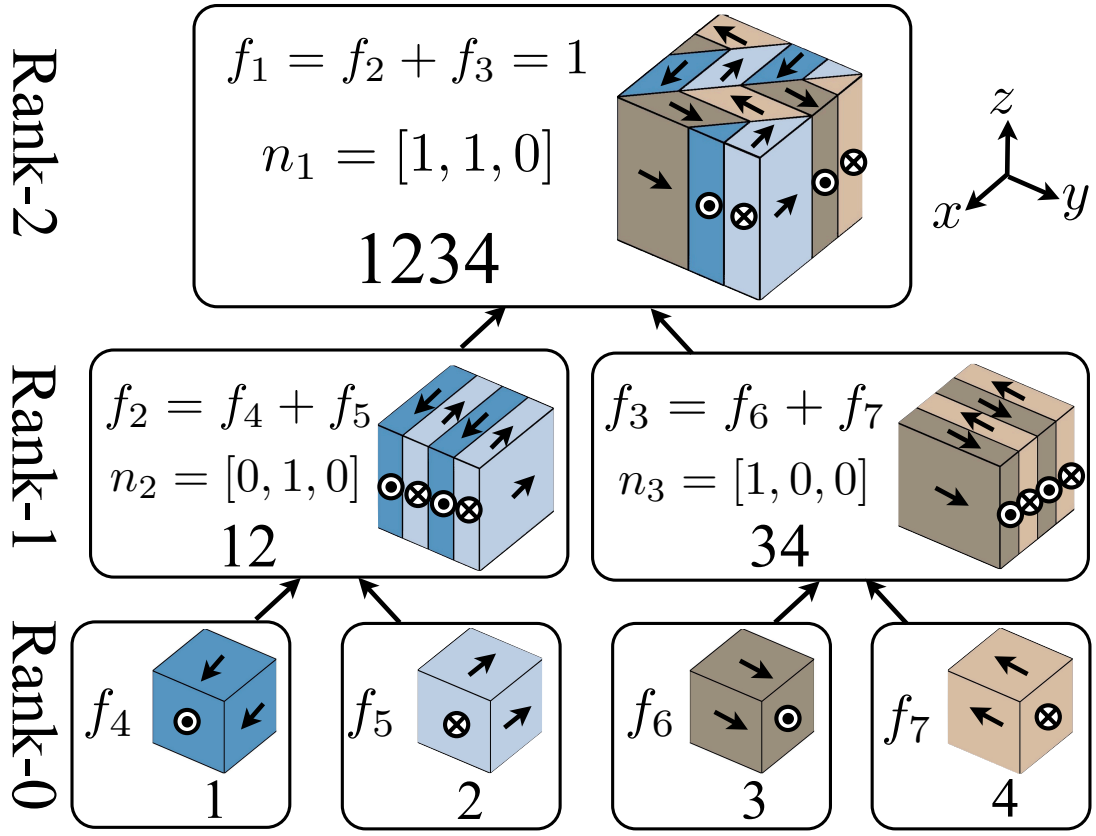

Figure 2.4: A schematic binary tree for rank-2 ($R = 2$) laminate domain pattern 1234 where f_i is the volume fraction associated with the ith node and $\mathbf{n}_i$ is the interface normal vector. Levels of the tree are numbered $r = 0 \ldots R$ corresponding to the rank of nodes at that level.

$l_1 > l_2 = l_3$, while a topologically equivalent structure shown in figure 2.5(b) has different domain spacing $l_1 < l_2 = l_3$. Since the domain topologies are independent to length scale l_i, in this work the domain structures are drawn in the way that nodes in the higher level of the tree have greater values of length scale than those in the lower level of the tree; all nodes in the same level of the tree have identical values of length scale, i.e. as the case shown in figure 2.5(a), $l_1 > l_2 = l_3$. Thus, we mainly treat length scale l_i as a drawing parameter and do not specify values during the majority of calculations in the present work.

Returning to the tree diagram, the ith node is associated with a volume fraction f_i, such that each parent node has volume fraction equal to the sum of those of its child nodes at the next level down.

$$f_i = f_{2i} + f_{2i+1} \qquad (i = 1 \ldots 2^R - 1) \tag{2.10}$$

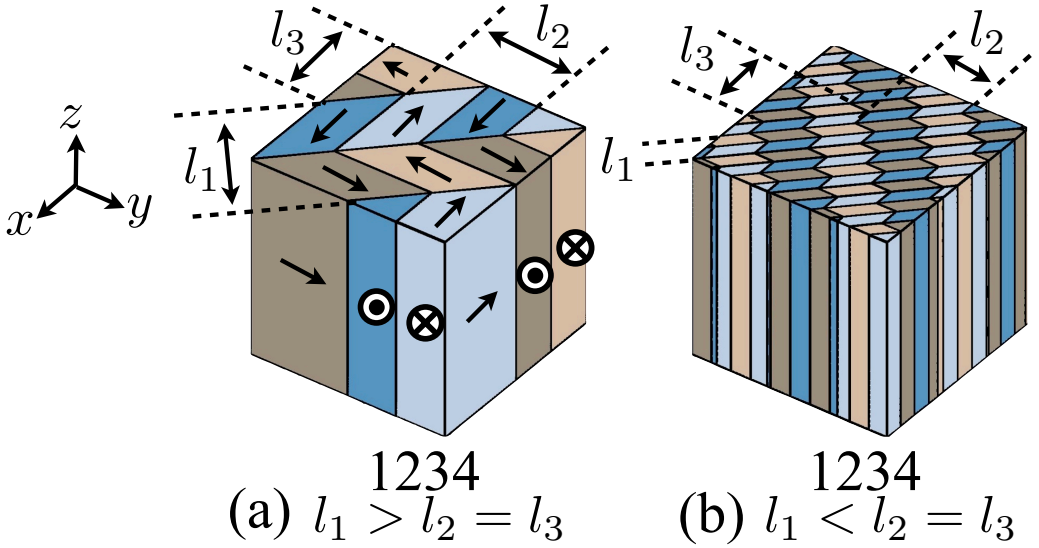

Figure 2.5: Equivalent domain topologies (a) Structure 1234. (b) Structure 1234 with domain spacing $l_1 < l_2 = l_3$.

Similarly, parent nodes have an average strain and polarization state that can be derived from those of its child nodes

$$\begin{aligned} \boldsymbol{\epsilon}_i &= f_{2i}\boldsymbol{\epsilon}_{2i} + f_{2i+1}\boldsymbol{\epsilon}_{2i+1} \\ \mathbf{p}_i &= f_{2i}\mathbf{p}_{2i} + f_{2i+1}\mathbf{p}_{2i+1} \end{aligned} \tag{2.11}$$

Information about the volume fractions of the individual crystal variants can be obtained by considering the macroscopic properties of the crystal. For example, when an average remanent strain $\boldsymbol{\epsilon}^r$ and average polarization $\mathbf{P}$ are specified by external boundary conditions, the total volume fraction $f_{(k)}$ of each pure variant can be determined. Here, the bracketed subscript has been introduced to indicate the total volume fraction $f_{(k)}$ of the kth crystal variant, which is different from the volume fraction f_i associated with node i in the tree diagram. Under the conditions of no internal charge and stress-free domain structure, the macroscopic values $\boldsymbol{\epsilon}^r$ and $\mathbf{P}$ are given by volume averages over the corresponding crystal variants. Thus

$$\boldsymbol{\epsilon}^r = \sum_{k=1}^{N} f_{(k)}\boldsymbol{\epsilon}_{(k)} \tag{2.12}$$

$$\mathbf{P} = \sum_{k=1}^{N} f_{(k)}\mathbf{p}_{(k)} \tag{2.13}$$

$$1 = \sum_{k=1}^{N} f_{(k)} \tag{2.14}$$

where N is the number of all variant types in the crystal system, and all $f_{(k)}$ are subjected to the condition $0 \leq f_{(k)}$. Note that equation (2.14) simply states that the volume fractions of all the crystal variants present must sum to unity.

Equation (2.12) can be derived as follows. Consider a crystal with a given macroscopic strain state ϵ_{ij}^{r}, which is associated with surface displacement $u_i = \epsilon_{ij}^{r} x_j$, where x_j is position vector of the surface of the crystal. The volume average of the local strain in the crystal can be expressed as $\frac{1}{V}\int_V \epsilon_{ij}^{local} \mathrm{d}V$, where V is the volume of the crystal. By using the relationship between displacement and local strain without rigid body rotation $u_{i,j} = \epsilon_{ij}^{local}$ and the divergence theorem, we can rewrite the average of the local strain as

$$\frac{1}{V}\int_V \epsilon_{ij}^{local} \mathrm{d}V = \frac{1}{V}\int_V u_{i,j} \mathrm{d}V = \frac{1}{V}\int_s u_i n_j \mathrm{d}s = \frac{1}{V}\int_s \epsilon_{ik}^{r} x_k n_j \mathrm{d}s \tag{2.15}$$

where s is the surface area of the crystal; n_j is the surface normal tensor of s. As the macroscopic strain ϵ_{ij}^{r} is independent of the surface integration, equation (2.15) then becomes

$$\frac{1}{V}\int_s \epsilon_{ik}^{r} x_k n_j \mathrm{d}s = \frac{1}{V}\epsilon_{ik}^{r}\int_V x_{k,j} \mathrm{d}V = \frac{1}{V}\epsilon_{ik}^{r}\delta_{kj} V = \epsilon_{ij}^{r} \tag{2.16}$$

Equations (2.15) and (2.16) show that the macroscopic strain is the average of the local strain. Furthermore, the local strain can also be expressed in terms of applied stress σ_{kl}, electric field E_k and local spontaneous remanent strain state ϵ_{ij}, giving

$$\epsilon_{ij}^{local} = s_{ijkl}^{E}\sigma_{kl} + d_{kij}E_k + \epsilon_{ij} \tag{2.17}$$

Consider a crystal which has an exactly compatible microstructure subjected to zero applied stress and electric field. The local strain ϵ_{ij}^{local} at a point in the crystal then equals the remanent

strain state of the crystal variant which occupies that point. Thus, we have

$$\epsilon_{ij}^{r} = \frac{1}{V}\int_{V} \epsilon_{ij} \mathrm{d}V \tag{2.18}$$

In laminate structures, equation (2.18) can be simplified to equation (2.12).

Equation (2.13) can also be derived in a similar way. Consider a crystal having a given macroscopic remanent polarization P_i. It is worth noting that the macroscopic remanent polarization is related to the macroscopic electric displacement by $\overline{D}_i = \kappa_0 E_i + P_i$, where κ_0 is the permittivity of free space. In ferroelectric materials, polarization P_i is typically at least two or three orders of magnitude greater than $\kappa_0 E_i$ [92]. Therefore P_i is approximated to $\overline{D}_i$. Next, the volume average of the local electric displacement D_i is given by

$$\frac{1}{V}\int_{V} D_i \mathrm{d}V = \frac{1}{V}\int_{V} D_j \delta_{ij} \mathrm{d}V = \frac{1}{V}\int_{V} D_j x_{i,j} \mathrm{d}V = \frac{1}{V}\int_{V} (D_j x_i)_{,j} - D_{j,j} x_i \mathrm{d}V \tag{2.19}$$

Under the conditions of no internal charge within the crystal, we can have $\nabla \cdot \mathbf{D} = D_{j,j} = 0$. Thus, equation (2.19) becomes

$$\frac{1}{V}\int_{V} (D_j x_i)_{,j} \mathrm{d}V = \frac{1}{V}\int_{s} D_j x_i n_j \mathrm{d}s \tag{2.20}$$

Since the electric displacement D_j on the surface s equals the macroscopic electric displacement $\overline{D}_j$ and is also independent of the surface integration, equation (2.20) then becomes

$$\frac{1}{V}\int_{s} D_j x_i n_j \mathrm{d}s = \frac{1}{V}\overline{D}_j \int_{s} x_i n_j \mathrm{d}s = \frac{1}{V}\overline{D}_j \int_{V} x_{i,j} \mathrm{d}V = \frac{1}{V}\overline{D}_j \delta_{ij} V = \overline{D}_i \tag{2.21}$$

Thus, the macroscopic electric displacement is the average of the local electric displacement. Again, the local electric displacement can be expressed in terms of σ_{kl}, E_k and remanent polarization p_i, giving

$$D_i = d_{ikl}\sigma_{kl} + \kappa_{ik}^{\sigma} E_k + p_i \tag{2.22}$$

Since a crystal subjected to zero external traction and applied voltage is considered here, the local electric displacement D_i at a point in the crystal is equal to the remanent polarization of the crystal variant which occupies that point. This gives us

$$P_i = \frac{1}{V}\int_V p_i \mathrm{d}V \tag{2.23}$$

In laminate structures, equation (2.23) can then be rewritten as equation (2.13).

Equations (2.12)–(2.14) typically correspond to a system of 10 linear equations; if these are invertible the total volume fractions of the variants can be obtained directly. However, these equations may be invertible, singular or overdetermined, depending on the particular variants in the crystal system. For example, the tetragonal crystal system of 6 variants, which is common in perovskite ferroelectrics, reduces these equations to exactly 6 independent linear equations for 6 unknown volume fractions. Thus, the volume fraction of each crystal variant can be uniquely determined. By contrast, rhombohedral phases have 8 crystal variants and only produce 7 independent linear equations for the volume fractions, so that there is one degree of freedom in determining the volume fractions. This problem is discussed further in chapter 3.

Assuming the total volume fractions of the variants are known, there remains the problem of constructing a compatible domain configuration–that is, distributing the volume fractions among the nodes of a tree diagram in such a way as to produce a compatible structure overall. In the following paragraphs, three types of compatibility are discussed: compatibility on average (COA), exact compatibility (EC) and disclination-free (DF) compatibility.

2.3.2 Compatibility on average (COA)

One strategy for minimising the functional $F(\mathbf{u}, \mathbf{p})$ is to assume that domains are arranged in a multi-rank laminate with a separation of length scales between successive levels of the tree diagram. Under this assumption, the material represented by each parent node can be treated as

a homogeneous medium with the strain and polarization states given by equation (2.11). Thus, the material represented by each node is a fine phase mixture [50] of the materials at its child nodes. In this way, compatibility can be achieved in a volume average sense that neglects the energy associated with fine scale local incompatibility across high level interfaces. In terms of a rank-R tree diagram, COA laminates achieve compatibility between nodes 2_i and $2i+1$ for all the parent nodes i in the range $1 \leq i \leq 2^R - 1$. Compatibility between other nodes is neglected.

The theory developed by Li and Liu [26], which is analogous to similar concepts of magnetic martensites by DeSimone and James [52], provides a general method for constructing multi-rank COA laminates in ferroelectric crystals with any given average strain and polarization states. In their work, certain special loading cases are considered which give sets of "energetically favoured" crystal variants. More generally, consider a macroscopic state of strain and polarization and solve equations (2.12)–(2.14) to produce a set of n non-zero volume fractions $f_{(i)}$ $(i = 1 \ldots n)$ in the crystal. According to the construction of Li and Liu [26], it is possible to form a domain configuration with the strain and polarization

$$\boldsymbol{\epsilon}^r = \mu_1 \boldsymbol{\epsilon}_{(1)} + \mu_2(1-\mu_1)\boldsymbol{\epsilon}_{(2)} + \cdots + \mu_{n-1} \prod_{m=1}^{n-2} (1-\mu_m)\boldsymbol{\epsilon}_{(n-1)} + \prod_{m=1}^{n-1} (1-\mu_m)\boldsymbol{\epsilon}_{(n)} \quad (2.24)$$

$$\mathbf{P} = \mu_1 \mathbf{p}_{(1)} + \mu_2(1-\mu_1)\mathbf{p}_{(2)} + \cdots + \mu_{n-1} \prod_{m=1}^{n-2} (1-\mu_m)\mathbf{p}_{(n-1)} + \prod_{m=1}^{n-1} (1-\mu_m)\mathbf{p}_{(n)} \quad (2.25)$$

where μ_m are coefficients related to the volume fractions $f_{(i)}$ as follows [52]

$$\mu_m = \begin{cases} 0, & \sum_{i=1}^{m-1} f_{(i)} = 1 \\ \dfrac{f_{(m)}}{1 - \sum_{i=1}^{m-1} f_{(i)}}, & \text{otherwise} \end{cases} \quad (2.26)$$

The coefficients μ_m are then used to specify a rank $n-1$ COA domain configuration as described below.

An example of a tree diagram corresponding to a rank-3 laminate generated by the procedure of Li and Liu is shown in figure 2.6. Suppose there are four energetically favoured variants ($f_{(k)} \neq 0,\ k = 1 \ldots 4$). Following equations (2.24)–(2.26), the resulting rank-3 laminate structure is ensured to satisfy the COA criteria by distributing the volume fraction of variant 1 across four nodes (node numbers 8, 10, 12, 14), and variant 2 across two nodes (node numbers 9, 13) at the lowest level of the tree. To understand this, figure 2.6 shows that the values of μ_1, μ_2 and μ_3 generated by equation (2.26) cause the volume fraction ratio between variant 1 and 2 at their parent node 4 to match exactly the volume fraction ratio between variants 1 and 3 at node 5. This guarantees that a COA laminate, represented by node 2, can be formed between the materials represented by nodes 4 and 5. It can be demonstrated as follows. According to figure 2.6, the average strain and polarization states of nodes 4 and 5 are

$$\boldsymbol{\epsilon}_4 = \frac{\mu_1\mu_2\mu_3}{\mu_2\mu_3}\boldsymbol{\epsilon}_{(1)} + \frac{(1-\mu_1)\mu_2\mu_3}{\mu_2\mu_3}\boldsymbol{\epsilon}_{(2)}, \quad \boldsymbol{\epsilon}_5 = \frac{\mu_1(1-\mu_2)\mu_3}{(1-\mu_2)\mu_3}\boldsymbol{\epsilon}_{(1)} + \frac{(1-\mu_1)(1-\mu_2)\mu_3}{(1-\mu_2)\mu_3}\boldsymbol{\epsilon}_{(3)}$$

$$\mathbf{p}_4 = \frac{\mu_1\mu_2\mu_3}{\mu_2\mu_3}\mathbf{p}_{(1)} + \frac{(1-\mu_1)\mu_2\mu_3}{\mu_2\mu_3}\mathbf{p}_{(2)}, \quad \mathbf{p}_5 = \frac{\mu_1(1-\mu_2)\mu_3}{(1-\mu_2)\mu_3}\mathbf{p}_{(1)} + \frac{(1-\mu_1)(1-\mu_2)\mu_3}{(1-\mu_2)\mu_3}\mathbf{p}_{(3)} \tag{2.27}$$

Thus, the left hand side of the compatibility equations (2.6) and (2.7) for nodes 4 and 5 are

$$\boldsymbol{\epsilon}_4 - \boldsymbol{\epsilon}_5 = \left[\mu_1\boldsymbol{\epsilon}_{(1)} + (1-\mu_1)\boldsymbol{\epsilon}_{(2)}\right] - \left[\mu_1\boldsymbol{\epsilon}_{(1)} + (1-\mu_1)\boldsymbol{\epsilon}_{(3)}\right] = (1-\mu_1)(\boldsymbol{\epsilon}_{(2)} - \boldsymbol{\epsilon}_{(3)})$$

$$\mathbf{p}_4 - \mathbf{p}_5 = \left[\mu_1\mathbf{p}_{(1)} + (1-\mu_1)\mathbf{p}_{(2)}\right] - \left[\mu_1\mathbf{p}_{(1)} + (1-\mu_1)\mathbf{p}_{(3)}\right] = (1-\mu_1)(\mathbf{p}_{(2)} - \mathbf{p}_{(3)}) \tag{2.28}$$

Consequently, the compatibility requirements for nodes 4 and 5 are equivalent to those for two pure crystal variants 2 and 3. As mentioned above, any single crystal variant can form a compatible interface with another single variant of the same crystal system in the considered cases. Thus, solutions for a compatible interface which separate nodes 4 and 5 are guaranteed to exist.

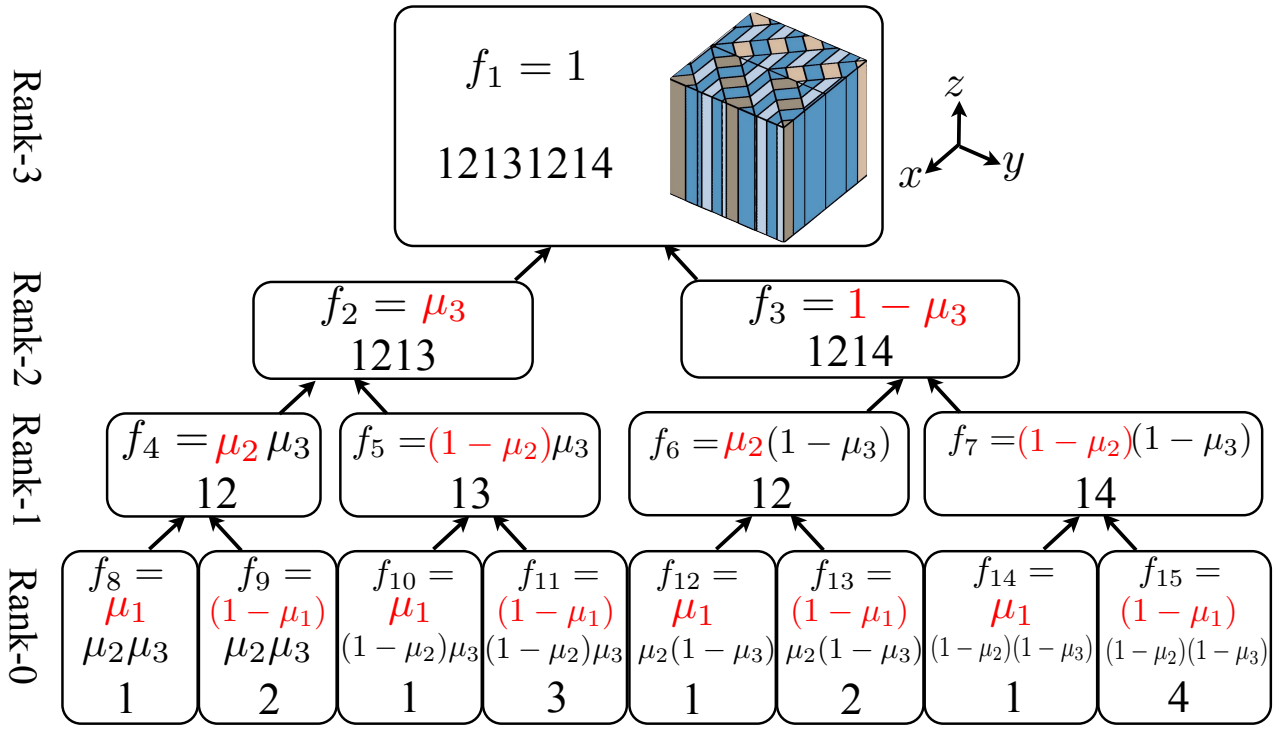

Figure 2.6: The domain configuration of a rank-3 laminate constructed by Li and Liu's method.

A similar pattern of COA lamination is generated throughout the tree diagram. It is worth noting that the variant 1 is distributed such that it is present in all four nodes in the rank-1 level of the tree. Similarly, variant 2 is present in all nodes at the rank-2 level. This elegant configuration ensures that every laminating process is equivalent to conjoining a pair of pure variants, since the sublaminates always contain common crystal variants whose strain and polarization states cancel in equations (2.6) and (2.7).

Although the construction described by Li and Liu [26] gives a general way of forming a laminate with a given macroscopic strain and polarization, it commonly results in high rank and locally incompatible structures. For example, the tree diagram in figure 2.6 has 4 variants and thus produces a rank-3 structure by the method of Li and Liu. However, returning to figure 2.4 it can be seen that a simpler, rank-2, arrangement of the same 4 variants is possible. It is often possible to find a lower rank lamination than that generated by the procedure of Li and Liu. Furthermore, the structure shown in figure 2.4 is exactly compatible at all interfaces; this type of compatibility allows low energy microstructures without requiring a separation of

length scales between successive levels of the binary tree, and motivates the development of the further criteria needed to define exactly compatible (EC) laminate.

2.3.3 Exact compatibility (EC)

Arlt and Sasko [1] identified two types of laminate structures in ferroelectric crystals: α-type structure, shown in figure 2.7(a), has one to one perfect domain alignment with "head to tail" polarization directions across interfaces, corresponding to exactly compatible (EC) structure. By contrast, the β-type structure (COA) in figure 2.7(b) has some regions with "head to head" or "tail to tail" polarization which violate equation (2.7). The incompatible interfaces are charged boundaries, and thus increase the total energy of the crystal. Both structures in figure 2.7 satisfy the criteria of compatibility on average, and we can consider that EC structure is a special case of COA structure. Considering a rank-R laminate, there are three criteria for achieving an EC domain configuration

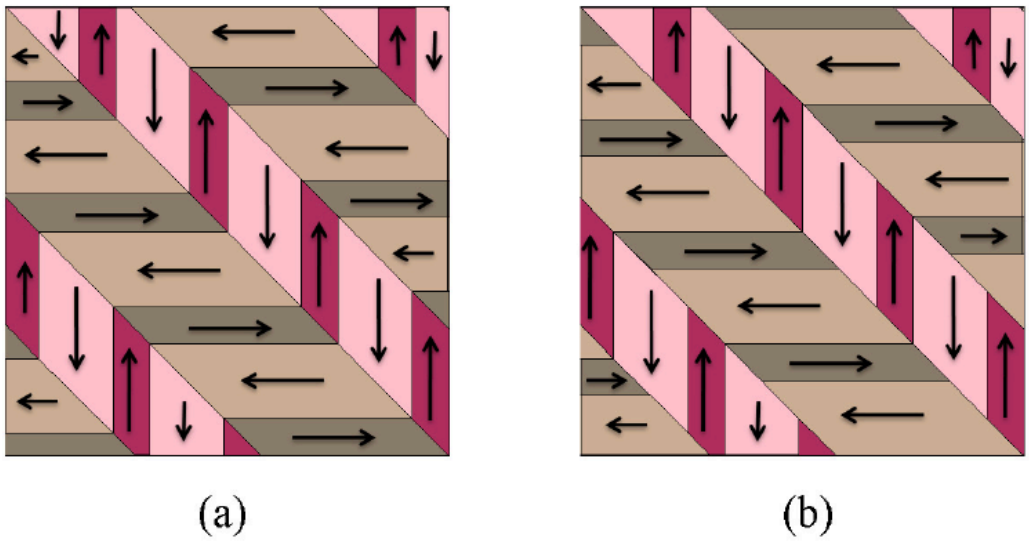

Figure 2.7: Rank-2 microstructures constructed with (a) exact compatibility and (b) compatibility on average.

(i) The condition of volume fraction ratio equivalence The volume fraction ratios of all domain pairs in a given level $r = 0 \ldots R-2$ must be identical

$$\frac{f_{2^{R-r}}}{f_{2^{R-r}+1}} = \frac{f_{2^{R-r}+2m-2}}{f_{2^{R-r}+2m-1}}, \qquad (m = 2 \ldots 2^{R-r-1}) \tag{2.29}$$

Here, 2^{R-r} is the first node number in level r of the tree, and the maximum value of m is the number of laminate pairs in level r. This condition ensures that domains that meet across a higher level interface have the same spacing on that interface. A similar constraint was described by Rodel [93]. Interestingly, the volume fraction arrangement proposed by Li and Liu can satisfy equation (2.29), as can be seen in the example tree diagram of figure 2.6. The condition of equation (2.29) vanishes in levels $r > R-2$, since there is then no higher level interface across which the domains meet.

(ii) The condition of interface normals A second requirement for an EC structure is that, where domain walls meet a higher level interface, their projection into that interface matches in orientation with the projection of the corresponding domain wall on the opposite side of the interface. This is illustrated in figure 2.8 where an EC structure of rank 3 is shown in figure 2.8(a), and the same structure is split open along the highest level interface in figure 2.8(b). In figure 2.8, arrows corresponding to the individual polarization directions of the domains are not shown; instead 6 colors/shades are used, corresponding to the 6 crystal variants of the tetragonal crystal system. It is shown that where the structure is split, the domain patterns exposed on the interface perfectly match. In terms of the tree diagram, for every child node, the projection of its interface normal vector onto all interfaces of its higher level parent nodes must be parallel to that of a corresponding child node on the opposite side of the tree. The relationship between the interface normal vectors of parent node $i = 1 \ldots 2^{R-1} - 1$ and every child node p and q must satisfy

$$(\mathbf{n}_p - (\mathbf{n}_p \cdot \mathbf{n}_i)\mathbf{n}_i) \times (\mathbf{n}_q - (\mathbf{n}_q \cdot \mathbf{n}_i)\mathbf{n}_i) = 0 \tag{2.30}$$

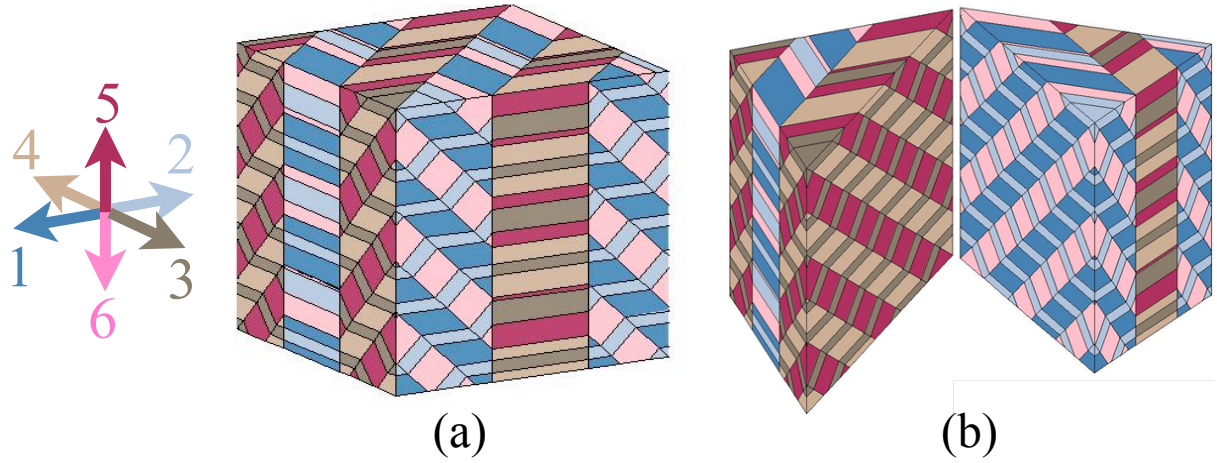

Figure 2.8: (a) An EC structure of rank-3 and (b) the structure split open along a high level interface showing a matching set of domain wall orientations.

which is equivalent to

$$(\mathbf{n}_p \times \mathbf{n}_q) \cdot \mathbf{n}_i = 0 \tag{2.31}$$

where the node numbers p and q are given by

$$p = 2^{j+1}i + k, \quad q = p + 2^j; \quad (j = 0 \ldots r-2, \quad k = 0 \ldots 2^j - 1) \tag{2.32}$$

In equation (2.32), the tree level of node i is r, given by $r = R - \lfloor \log_2 i \rfloor$, where $\lfloor x \rfloor$ indicates the greatest integer less than or equal to x. For an EC structure, equation (2.31) must be satisfied over all possible permutations of j and k. This criterion ensures that all layers and their sub-layers have the same orientation on their common interface. Thus, a microstructure can have "one to one" matched domain configuration if its corresponding tree diagram satisfies the first and second conditions provided by equations (2.29) and (2.31).

(iii) The condition of compatibility between adjacent domains Even though geometrically matched structures are achieved by having equal domain spacing and orientation, local strain and polarization compatibility requirements still need to be satisfied. This avoids incompatibilities such as "head to head" polarizations. Thus, a third condition for an EC structure is that all pairs of adjacent domains must satisfy compatibility across the higher rank interface that sep-

arates them. Again, this condition can be expressed in terms of the nodes of the tree diagram. The interface normal vector $\mathbf{n}_i$ $(i = 1 \dots 2^R - 1)$ of each parent node i (layer r) and the strain and polarization states ($\boldsymbol{\epsilon}_p$, $\boldsymbol{\epsilon}_q$, $\mathbf{p}_p$, $\mathbf{p}_q$) of the pure crystal variants at node numbers p and q in the bottom level (rank-0) of the tree must satisfy

$$\boldsymbol{\epsilon}_p - \boldsymbol{\epsilon}_q = \frac{1}{2}(\mathbf{a} \otimes \mathbf{n}_i + \mathbf{n}_i \otimes \mathbf{a}) \tag{2.33}$$

$$(\mathbf{p}_p - \mathbf{p}_q) \cdot \mathbf{n}_i = 0 \tag{2.34}$$

In this case, the node numbers p, q are given by

$$p = 2^r i + k, \quad q = p + 2^{r-1}; \quad (k = 0 \dots 2^{r-1} - 1, \quad r = R - \lfloor \log_2 i \rfloor) \tag{2.35}$$

These three exact compatibility conditions, equations (2.29), (2.31) and (2.33)–(2.34), define periodic multi-rank laminate structures without local incompatibility, i.e. compatible at all interfaces: they minimise the energy $F(\mathbf{u}, \mathbf{p})$ without the need for separation of length scales. It is interesting to note that another method for finding compatible laminates is also presented in Shu and Bhattacharya [24]. Their results satisfy the condition (i) but do not satisfy conditions (ii) and (iii) in general.

2.3.4 Geometric analogy with the R-cube

The relations between domains in a rank-R exactly compatible laminate structure can be described with a geometric analogy. The rank-R laminate has 2^R nodes in the lowest level of its binary tree, each of which represents a single domain that forms compatible interfaces with R other domains. The nodes of the lowest tree level are analogous to the 2^R vertices of a cube in R-dimensions, while the $2^{R-1}R$ edges of the R-cube correspond to the set of domain walls. It is possible to distort the R-cube such that each edge lies parallel to the interface normal of the

corresponding domain wall. For example, a rank-2 laminate is analogous to a trapezium with two parallel edges. The parallel edges represent the highest level interface normal, which is shared by two pairs of domains. Equation (2.30) constrains the interface normals at child nodes p, q and at parent node i to lie in plane, for node numbers p, q and i drawn from equation (2.32), resulting in a closed figure. Compatibility of adjacent domains (see equations (2.6) and (2.7)) further restricts the directions in which the cube edges may lie.

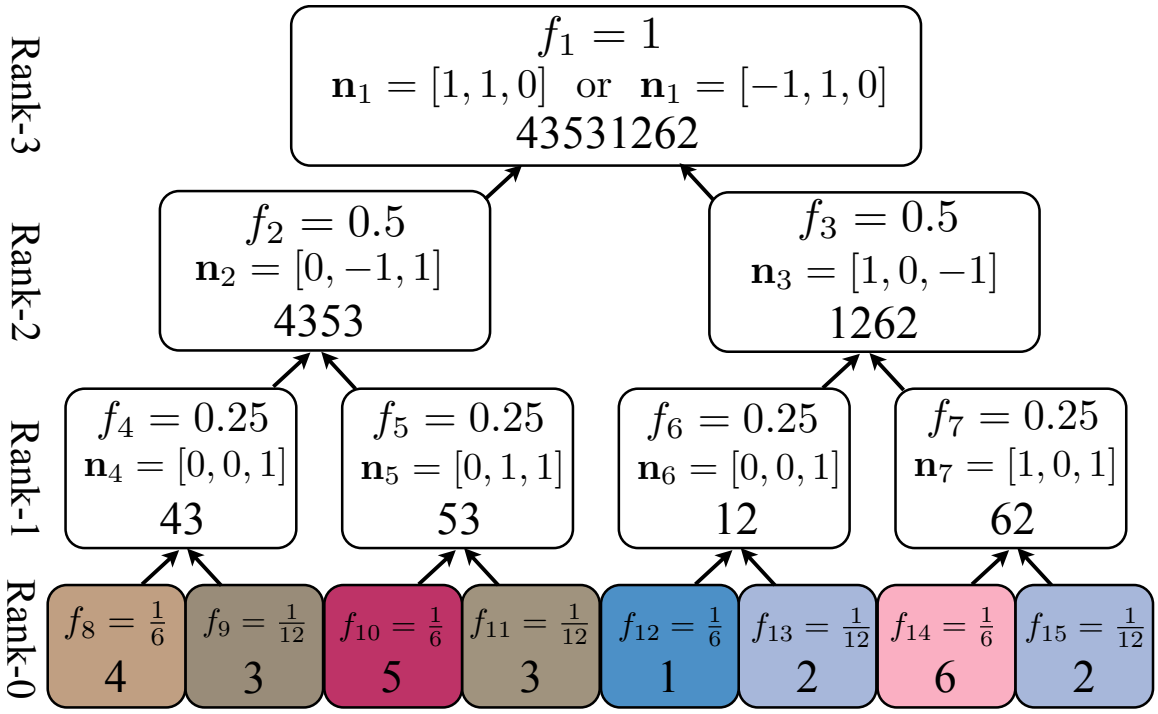

Figure 2.9: The binary tree structure of a rank-3 laminate which consists of multiple choices of the highest interface normal $\mathbf{n}_1$.

Figure 2.9 is an example of rank-3 tree diagram which can form either COA or EC domain configurations depending on the choice of the highest interface normal $\mathbf{n}_1$ since both values of $\mathbf{n}_1$ given in figure 2.9 satisfy equations (2.6) and (2.7). This non-uniqueness of microstructures will be discussed in more detail in section 3.2. For present purposes, the tree diagram in figure 2.9 can be used to help understand the R-cube analogy. Distorted 3-dimensional cubes reveal the relationship between the interface normals of the laminations corresponding to node pairs 4 and 5, 6 and 7, 4 and 6, 5 and 7, 2 and 3. The COA laminate produced by choosing

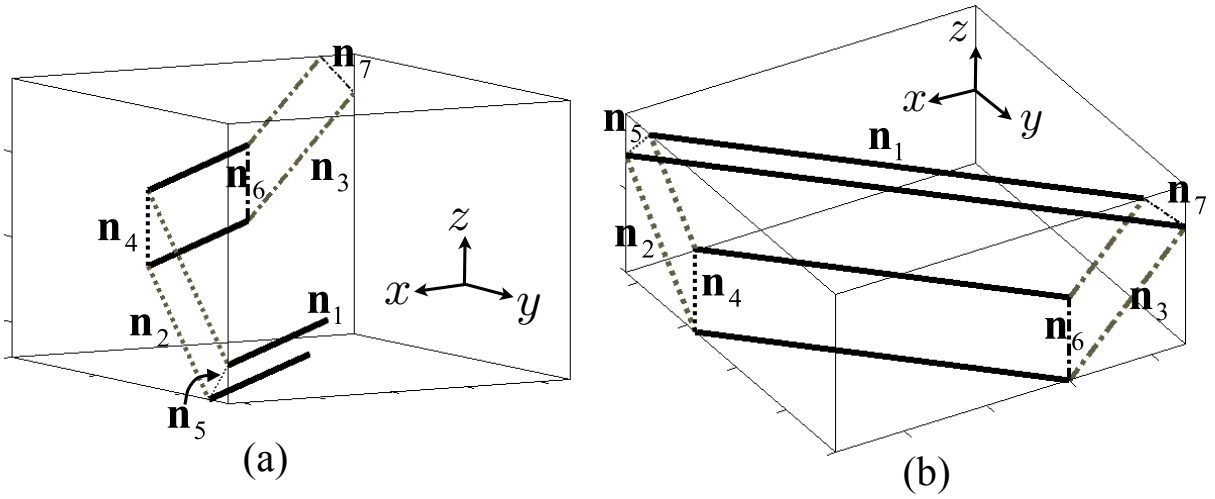

Figure 2.10: Geometric analogy for a rank-3 laminate with (a) COA, $\mathbf{n}_1 = [1, 1, 0]$, and (b) EC, $\mathbf{n}_1 = [-1, 1, 0]$, configurations of the binary tree shown in figure 2.9.

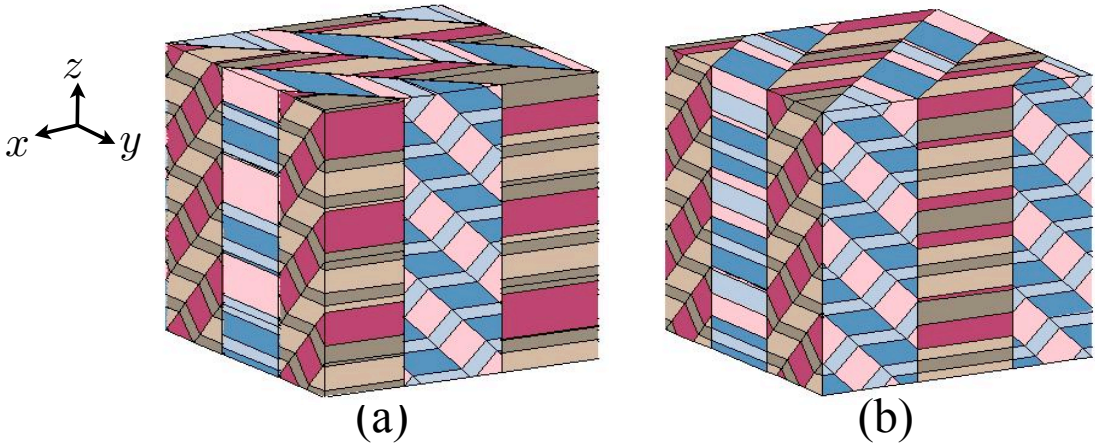

Figure 2.11: The (a) COA, $\mathbf{n}_1 = [1, 1, 0]$, and (b) EC, $\mathbf{n}_1 = [-1, 1, 0]$, domain configurations of the binary tree shown in figure 2.9.

$\mathbf{n}_1 = [1, 1, 0]$ in figure 2.9 gives rise to an open figure as shown in figure 2.10(a). This COA domain configuration is shown in figure 2.11(a). The open figure happens because interface normals $\mathbf{n}_1$, $\mathbf{n}_2$, $\mathbf{n}_3$ are not coplanar; $\mathbf{n}_1$, $\mathbf{n}_5$, $\mathbf{n}_7$ are also not coplanar, causing the two surfaces which consist of $\mathbf{n}_2$, $\mathbf{n}_4$, $\mathbf{n}_5$ and $\mathbf{n}_3$, $\mathbf{n}_6$, $\mathbf{n}_7$ to have different projections on a plane normal to the highest level interface normal $\mathbf{n}_1$. By contrast, the EC laminate produced by choosing $\mathbf{n}_1 = [-1, 1, 0]$ has an analogous distorted cube as shown in figure 2.10(b). The corresponding EC domain configuration is shown in figure 2.11(b). The two surfaces which consist of $\mathbf{n}_2$, $\mathbf{n}_4$, $\mathbf{n}_5$ and $\mathbf{n}_3$, $\mathbf{n}_6$, $\mathbf{n}_7$ in figure 2.10(b) have identical orientation with those in figure 2.10(a), how-

ever, $\mathbf{n}_1$ allows the two surfaces to have the same projection which makes the distorted R-cube close. The analogy with the R-cube provides a geometric way to view the necessary conditions on the interface normals in EC structures. However, note that there is no information about the volume fraction ratios in the analogy.

2.3.5 Disclination-free compatibility (DF)

Next consider the compatibility issues arising due to the disclination associated with certain domain junctions. Let the true rotation of the crystal lattice across a given domain wall be θ^r. The angles θ^r in several ferroelectric crystal systems are given in the work of Shu and Bhattacharya [24]. The net rotation of lattice planes, θ, where the pair of crystal variants i and j meet, is given by

$$\theta = \theta^r - \cos^{-1}(\hat{\mathbf{p}}_i \cdot \hat{\mathbf{p}}_j) \tag{2.36}$$

where $\hat{\mathbf{p}}_i$ and $\hat{\mathbf{p}}_j$ are the unit vectors along the pair of the idealized polarization directions in the reference frame of one of the crystal variants. When several domains are assembled into a composite, disclinations can be produced. Absence of disclinations is an additional constraint which must be satisfied for perfect compatibility of a laminate. Fousek and Mokry [53] studied the total disclination at the junction of groups of four domains. No disclination-free grouping was possible in the particular crystal system that they were considering. More generally, though, arrangements of domains that fit together perfectly, can be found in some crystal systems. The term disclination-free (DF) is used here for those laminate structures in the class EC that also satisfy the conditions required to fit together without disclinations.

To illustrate the disclination, consider tetragonal barium titanate, in which there is a shear strain of magnitude about 1% [1] between 90° domains. Careful consideration of the crystal structure near a 90° domain wall in this material shows that the crystal lattice rotates through 90.62° [24] across the wall. The wall contributes 0.62° to the disclination formed at the junction of four 90° domain walls. By contrast, there is no disclination contribution from a 180°

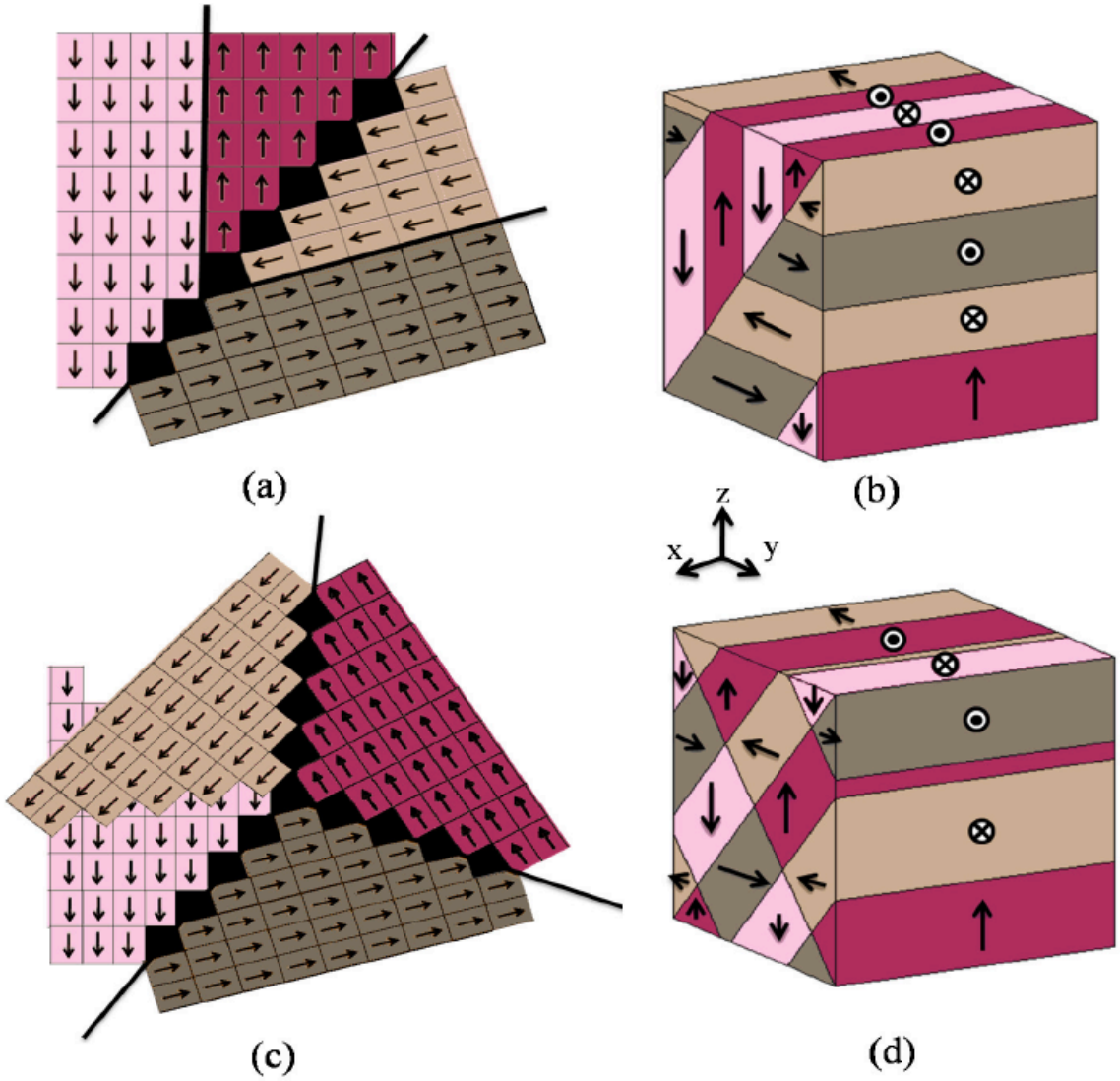

Figure 2.12: Disclinations in rank-2 structures: (a) a disclination-free structure, and (b) a corresponding laminate configuration; (c) a disclination at the junction of four domains, showing a relaxed state with domains overlapping and (d) a corresponding laminate configuration, in stressed state.

domain wall: the polarization turns through exactly 180° and the crystal lattice planes are continuous. Figure 2.12(a) shows a group of four domains in a DF configuration, with the lattice rotation exaggerated. This configuration is readily extended to form a rank-2 DF laminate (see figure 2.12(b)). By contrast, the group of four domains shown in figure 2.12(c) produces a disclination. They are shown in a relaxed state, producing an overlap at one domain wall. The group can be fitted together in a closed continuous form only by deforming the crystal lattice,

introducing stress or electric field. The corresponding laminate structure, figure 2.12(d), is EC but not DF. However, it could still exist in a real material: it could even be a minimum energy state for certain boundary conditions. Structures of this type, known as a polarization vortex, have been observed in nanoscale ferroelectrics [94] and are also predicted by simulations such as phase field and *ab initio* models [9, 14, 56]. Savytskii and Bismayer [54] examined the strain state at a single junction in a multi-domain configuration. They provide a condition for strain free configurations of domains meeting at a line. A similar condition was given by Shu and Bhattacharya [24]. The present work is concerned with finding DF multi-rank laminate structures and thus the global compatibility of an arrangement of domains must be considered. By using the tree diagram, the junctions of domains in a multi-rank laminate can be identified, and thus the full set of domain junctions in the structure can be taken into account, as follows.

In an EC structure, a pair of domains p, q which are children of node i in level $r = 1$, can be rotated from the ideal, or reference lattice configuration, into their exact configuration by a rotation $\mathbf{R}_i$ about the axis $\mathbf{p}_p \times \mathbf{p}_q$ satisfying

$$\cos^{-1}(\mathbf{R}_i \mathbf{p}_p \cdot \mathbf{R}_i^{-1} \mathbf{p}_q) = \theta^r_{p,q} \tag{2.37}$$

where p and q are node numbers generated from equation (2.35); $\theta^r_{p,q}$ is the true rotation of lattice planes at the domain wall between domains p and q in a stress-free configuration. Rotation $\mathbf{R}_i$ turns the polarizations at nodes p and q in opposite senses around the same axis. A similar rotation can be carried out at all pairs of nodes in the lowest level of the tree diagram, producing a new, rotated set of strain and polarization states for each domain. At higher levels of the tree, further conditions arise, as discussed in section 2.3.3, because of domains meeting across high level interfaces. Then for each node i in levels $r = 2 \ldots R$, a rotation matrix $\mathbf{R}_i$ must be found that satisfies equation (2.37), and additionally the rotated interface normals must align, giving a

condition similar to equation (2.31)

$$(\mathbf{R}_i \mathbf{n}_s \times \mathbf{R}_i^{-1} \mathbf{n}_t) \cdot \mathbf{n}_i = 0 \tag{2.38}$$

For all node numbers s and t in the set

$$s = 2^{j+1} i + k, \quad t = s + 2^j; \quad (j = 0 \ldots r-2, \quad k = 0 \ldots 2^j - 1) \tag{2.39}$$

A matrix $\mathbf{R}_i$ that satisfies conditions (2.37)–(2.39) can counter-rotate the laminates meeting across the interface defined at node i into a compatible DF configuration. However, this rotation could disturb the strain compatibility across the domain wall if the axis of rotation is not perpendicular to the interface normal $\mathbf{n}_i$. Thus, in addition to equation (2.38), the compatibility between adjacent domains (equations (2.6) and (2.7)) must be checked after the rotation. In general, equations (2.37)–(2.39) are strongly overdetermined and solutions only exist in special cases. Some examples of rank-2 DF structures are discussed in chapter 3. Examples of DF structures of rank greater than 2 were also found, though these typically were not the lowest rank structures for the given macroscopic state of strain and polarization.

It is worth noting that all of the conditions of microstructural compatibility described in sections 2.3.3 and 2.3.5 are independent of length scale. In sufficiently fine-scale microstructure, the domain wall energy becomes non-negligible and can control spacing. In coarser microstructure the interaction of disclination fields may play a key role in spacing. However, these interactions are neglected in the present work; compatible structural states are "designed" without specifying precise scale limitations. Observations of domain structure suggest that domain wall spacings arise naturally with a wide range of length scales, covering a range of 10^{-6} m to 10^{-2} m or more [5, 58].

3

Application to ferroelectric bulks and classification of laminate microstructures

3.1 Minimum rank laminates

Under the assumption of separation of length scales, high rank domain structures result in very fine domains, such that the domain wall energy in equation (2.1) becomes significant. Moreover, high rank structures often cannot satisfy exact compatibility conditions, leading to high energy states. While the model of Li and Liu [26] gives rank $n-1$ structures when there are n crystal variants present, the minimum possible rank is $\lceil \log_2 n \rceil$, where $\lceil x \rceil$ indicates the least integer greater than or equal to x. Thus there is the potential to find structures of lower rank than that of the Li-Liu construction whenever $n \geq 4$. Li and Liu [26] also mentioned that it is possible to find some low rank domain structures corresponding to special states of strain and polarization. They also stated that low rank domain structures are more likely to occur in real crystals, and that their calculated effective moduli have better agreement with experimental measurement than those of higher rank structures in the cases they considered.

Figure 3.1(a) shows an example of a rank-5 laminate which is a COA structure for a tetragonal crystal. This structure was determined using the model of Li and Liu, by setting the average strain and polarization of the entire crystal to zero; this models the unpoled state of

the material, as cooled from above the Curie temperature. In figure 3.1(a), this rank-5 structure contains such fine domains that the lowest rank divisions are barely visible. Figure 3.1(b) and (c) show two alternative configurations for this state of strain and polarization: figure 3.1(b) is a rank-3 COA structure, while figure 3.1(c) is a rank-3 EC structure. Of these three possible structures, it is expected that figure 3.1(c) represents the lowest energy state. In order to discover other low energy structures, a systematic procedure was developed to search for minimum rank domain configurations which satisfy the criteria of exact compatibility or disclination-free compatibility.

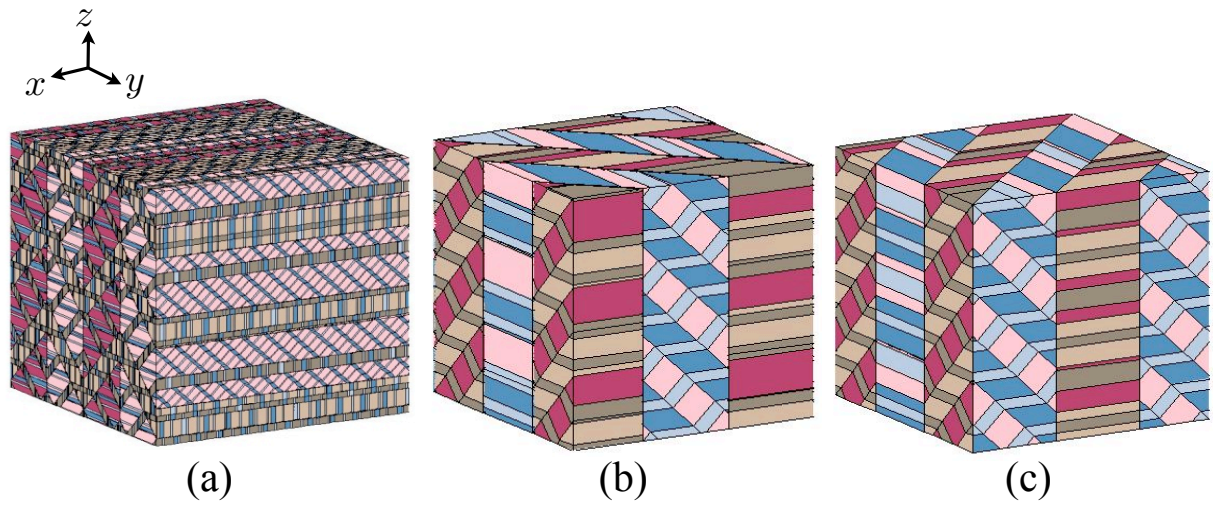

Figure 3.1: A tetragonal crystal with all 6 variants present can be constructed by (a) rank-5 compatibility on average (b) rank-3 compatibility on average and (c) rank-3 exact compatibility.

3.2 Method

The problem to be solved may be stated as follows: Let a ferroelectric single crystal within a given crystal system have average remanent strain $\boldsymbol{\epsilon}^r$ and average polarization $\mathbf{P}$. We seek an exactly compatible multi-rank laminate comprising the corresponding crystal variants with the given average strain and polarization state, and with minimum rank. The flow chart of the overall iteration process is shown in figure 3.2.

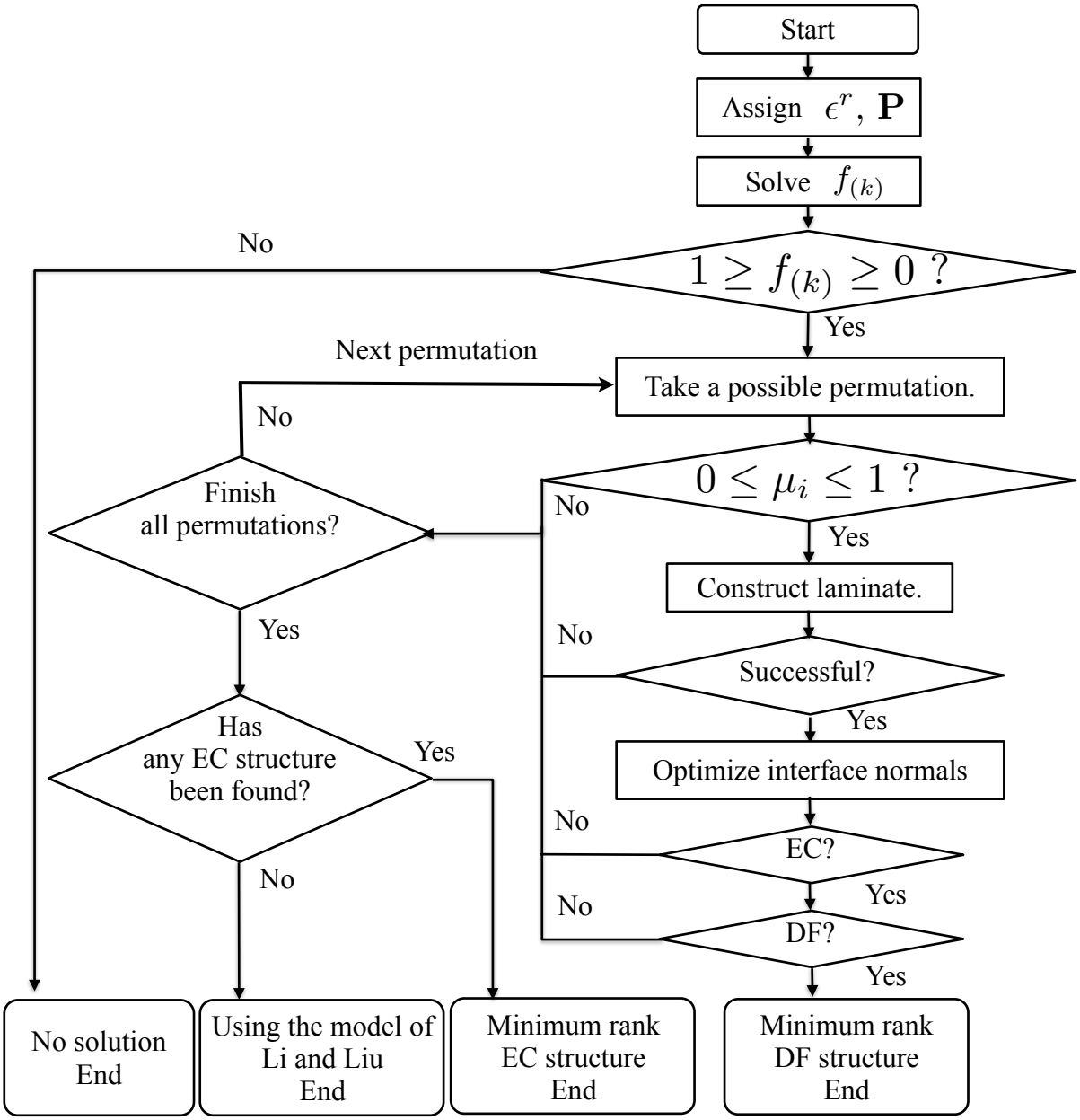

Figure 3.2: The flow chart of the iteration process for searching minimum rank EC or DF structures.

First, the macroscopic $\boldsymbol{\epsilon}^r$, $\mathbf{P}$ of the crystal and microscopic $\boldsymbol{\epsilon}_{(k)}$, $\mathbf{p}_{(k)}$ of pure variants, corresponding to the crystal system, are substituted into equations (2.12)–(2.14). If the solution $f_{(k)}$ exists and all $1 \geq f_{(k)} \geq 0$, the total volume fractions of all crystal variants can be obtained. It is worth noting that equations (2.12)–(2.14) can give us no solution, a unique solution, or a set of continuous solutions. Let n be the number of variants with their volume fraction greater than zero, which means there are n distinct variants present in the single crystal. Each of these

Table 3.1: The list of variant permutation for a 4 variants rank-2 structure.

Node in the lowest level	Node 4	Node 5	Node 6	Node 7
Variant order	“ 1	2	3	4 ”
	“ 1	2	4	3 ”
	“ 1	3	2	4 ”
	“ 1	3	4	2 ”
	“ 1	4	2	3 ”
	“ 1	4	3	2 ”

crystal variants has a “variant number”. For example, if $n = 4$ the variants may be 6, 4, 1, 3. However, for manipulation, a new labelling with “variant order numbers” is introduced, so that the corresponding variant order numbers run $1,\ 2 \ldots,\ n$. Now consider distributing the volume fractions of these n variants into $2^{\lceil \log_2 n \rceil}$ parts to fill the lowest level of a minimum rank binary tree diagram. A list of the set of variant permutations is first generated. For example, when the number of variants $n = 4$, there are $4! = 24$ possible permutations of the variants to fill into 4 nodes in the lowest level of a rank-2 tree. However, some of these permutations are equivalent due to the identical relative position of variants in the tree diagram (e.g. variant orders “1234”, “2143”, “3412” and “4321” produce identical structures). Note that variant order numbers are used here. For example, variant order number “1” indicates the first variant present in the list of variants with non-zero volume fraction. The six distinct permutations for a 4 variants rank-2 structure are listed in table 3.1. Whenever $2^{\lceil \log_2 n \rceil} > n$ there is freedom over how the volume fractions are divided among the nodes at the lowest level of the tree because at least one variant must have its volume fraction split between more than one node. There are then more complicated multiple permutations of the volume fraction arrangement. For example, when the number of variant present $n = 7$, one of the 7 variants needs to be divided into two parts in order to fill into 8 nodes in the lowest level of a rank-3 tree. Thus, after eliminating the equivalent permutations, there are in total 17640 possible permutations of variant arrangement, such as the variant order “11234567”, “12234567”... and so forth. The permutations are readily generated by computer.

The requirements of exact compatibility, equation (2.29), constrain the distribution of volume fractions. For example, in a rank-3 construction, the volume fractions must have the form: $\mu_1\mu_2\mu_3$, $(1-\mu_1)\mu_2\mu_3$, $\mu_1(1-\mu_2)\mu_3$, $(1-\mu_1)(1-\mu_2)\mu_3$, $\mu_1\mu_2(1-\mu_3)$, $(1-\mu_1)\mu_2(1-\mu_3)$, $\mu_1(1-\mu_2)(1-\mu_3)$, and $(1-\mu_1)(1-\mu_2)(1-\mu_3)$ in nodes 8 to 15 respectively. Here μ_i has the same meaning as defined in section 2.3.2, equations (2.24)–(2.26). For each permutation of the split volume fractions, a set of n simultaneous nonlinear equations in μ_i can be found to ensure that the nodal volume fractions consistently sum to the variant volume fractions. In general, for a rank-R laminate, these equations of volume fraction continuity may be written as

$$f_{(i)} = \sum_{j=2^R}^{2^{R+1}-1} C_{ij} f_j \tag{3.1}$$

where C_{ij} is a permutation matrix such that $C_{ij} = 1$ if the crystal variant at node j is variant number i and zero otherwise. The nodal volume fractions f_j are given by

$$f_j = \prod_{k=1}^{R} (1-2b)\mu_k + b \tag{3.2}$$

where

$$b = \left\lfloor \frac{j-2^R}{2^{k-1}} \right\rfloor - 2\left\lfloor \frac{j-2^R}{2^k} \right\rfloor \tag{3.3}$$

The binary digit b takes on a value of zero or unity depending on whether the jth node is reached by taking the left hand or right hand fork at the level $r = k-1$ of the binary tree. The nonlinearity of equations (3.1)–(3.3) can cause significant complication; however, the appearance of common factors of μ_i in these equations commonly simplifies the solution process.

A systematic search of the set of permutations is made, in each case checking for a consistent solution to equations (3.1)–(3.3). If a solution exists, the resulting arrangement is taken forward as a candidate structure and the remaining criteria for EC structure (equations (2.6), (2.7), (2.29), (2.30) and (2.33)–(2.35)) are checked. In addition, it is possible that equations (2.6) and

(2.7) allow a domain wall orientation to have two solutions or a set of continuous solutions, as is the case for 180° domain walls. This provides extra degrees of freedom that can allow the EC conditions to be satisfied. Thus this flexibility increases the chance of satisfying all the conditions of exact compatibility. For example, the domain structure shown in figure 3.1(c) is a typical case of minimum rank EC configuration in a tetragonal crystal system; in this case $\boldsymbol{\epsilon}^r = \mathbf{0}$ and $\mathbf{P} = \mathbf{0}$ which results in all six crystal variants being present, each with equal volume fraction $1/6$. It is worth noting that the laminates shown in figure 3.1(b) and figure 3.1(c) have exactly the same variants and volume fractions at every node of the tree diagram; the corresponding tree diagram was shown in figure 2.9. The only difference between these two structures is that the interface normal vectors of the structure in figure 3.1(b) do not satisfy the EC conditions.

In practice, where an extra degree of freedom arises, it normally allows equation (2.30) to be solved directly to obtain an optimised interface normal which satisfies the exact compatibility condition. Consider node p with a set of continuous solutions of interface normal $\mathbf{n}_p$. A unique $\mathbf{n}_p$ can be determined by solving equation (2.30) with adjacent nodes q drawn from equation (2.32). Here, note that, of all possible nodes q, this method requires that at least one of them has a unique solution for $\mathbf{n}_q$; otherwise, $\mathbf{n}_p$ cannot be solved by equation (2.30). If all the possible nodes q in equation (2.32) have non-unique $\mathbf{n}_q$, an alternative approach can be taken by solving equation (2.31) to find a $\mathbf{n}_p$ which is coplanar with $\mathbf{n}_{2p}$ and $\mathbf{n}_{2p+1}$. Finally, if this process does not uniquely specify $\mathbf{n}_p$, then $\mathbf{n}_p$ is chosen arbitrarily from the set of solutions. Following the flow chart shown in figure 3.2, minimum rank EC structures are generated systematically for a given state of strain and polarization; the DF criteria can also be checked during the iteration process.

3.3 Application to tetragonal ferroelectric bulks

A tetragonal crystal has six crystal variants in three pairs of opposite polarization. The strain states $\boldsymbol{\epsilon}_{(i)}, (i = 1 \ldots 6)$ and corresponding polarization states $\mathbf{p}_{(i)}$ are given by:

$$\boldsymbol{\epsilon}_{(1,\,2)} = \begin{bmatrix} \beta^t & 0 & 0 \\ 0 & \alpha^t & 0 \\ 0 & 0 & \alpha^t \end{bmatrix}, \quad \mathbf{p}_{(1,\,2)} = \pm \begin{bmatrix} p^t \\ 0 \\ 0 \end{bmatrix}$$

$$\boldsymbol{\epsilon}_{(3,\,4)} = \begin{bmatrix} \alpha^t & 0 & 0 \\ 0 & \beta^t & 0 \\ 0 & 0 & \alpha^t \end{bmatrix}, \quad \mathbf{p}_{(3,\,4)} = \pm \begin{bmatrix} 0 \\ p^t \\ 0 \end{bmatrix} \tag{3.4}$$

$$\boldsymbol{\epsilon}_{(5,\,6)} = \begin{bmatrix} \alpha^t & 0 & 0 \\ 0 & \alpha^t & 0 \\ 0 & 0 & \beta^t \end{bmatrix}, \quad \mathbf{p}_{(5,\,6)} = \pm \begin{bmatrix} 0 \\ 0 \\ p^t \end{bmatrix}$$

Here α^t, β^t and p^t are material properties; the superscript t indicates the tetragonal crystal system. There is choice over the reference state from which strains are measured. Strains of the unit cell can be defined relative to a cubic state of equal volume, such that $\text{tr}(\boldsymbol{\epsilon}) = 0$ and $\alpha^t = -\beta^t/2$. The true polarization rotation angle θ^r of the crystal lattice at a 90° domain wall is then [24]:

$$\theta^r = 2\tan^{-1}\left(\frac{1+\beta^t}{1-\beta^t/2}\right) \tag{3.5}$$

The net rotation of lattice planes at the domain wall can be calculated by using equation (2.36).

In the tetragonal system, equations (2.12)–(2.14) give

$$\begin{bmatrix} p^t & -p^t & 0 & 0 & 0 & 0 \\ 0 & 0 & p^t & -p^t & 0 & 0 \\ 0 & 0 & 0 & 0 & p^t & -p^t \\ \beta^t & \beta^t & \frac{-\beta^t}{2} & \frac{-\beta^t}{2} & \frac{-\beta^t}{2} & \frac{-\beta^t}{2} \\ \frac{-\beta^t}{2} & \frac{-\beta^t}{2} & \beta^t & \beta^t & \frac{-\beta^t}{2} & \frac{-\beta^t}{2} \\ \frac{-\beta^t}{2} & \frac{-\beta^t}{2} & \frac{-\beta^t}{2} & \frac{-\beta^t}{2} & \beta^t & \beta^t \\ 1 & 1 & 1 & 1 & 1 & 1 \end{bmatrix} \begin{bmatrix} f_{(1)} \\ f_{(2)} \\ f_{(3)} \\ f_{(4)} \\ f_{(5)} \\ f_{(6)} \end{bmatrix} = \begin{bmatrix} P_1 \\ P_2 \\ P_3 \\ \epsilon^r_{11} \\ \epsilon^r_{22} \\ \epsilon^r_{33} \\ 1 \end{bmatrix} \tag{3.6}$$

Note that the components in the row associated with macroscopic strain ϵ^r_{33} are linearly dependent on those of ϵ^r_{11} and ϵ^r_{22}, since $\text{tr}(\boldsymbol{\epsilon}) = 0$ is assumed. Thus, the 7×6 matrix in equation (3.6) which links volume fraction $f_{(k)}$ and macroscopic strain and polarization $[\mathbf{P}, \boldsymbol{\epsilon}^r]^T$ is of rank 6. Consequently, there are six equations for six unknown volume fractions giving a unique solution for the total volume fractions of each of the six crystal variants.

Consider applying the method described in section 3.2 to study the practical problem of poling a ferroelectric single crystal. Poling is an important procedure which alters the macroscopic properties of the crystal by rearranging its domain configuration. A natural question is whether there exists a continuous path that the microstructure may follow, from an initial, unpoled state ($P_1 = P_2 = P_3 = 0;\ \epsilon^r_{11} = \epsilon^r_{22} = \epsilon^r_{33} = 0$) to a fully poled, single variant state ($P_1 = P_2 = 0,\ P_3 = p^t;\ \epsilon^r_{11} = \epsilon^r_{22} = -\beta^t/2,\ \epsilon^r_{33} = \beta^t$). If such a path exists, what is the minimum rank route to poling? In order to resolve this question in the tetragonal crystal system it is instructive to explore the polarization-strain space ($P_3,\ \epsilon^r_{11},\ \epsilon^r_{33}$) with $P_1 = P_2 = 0,\ P_3 \geq 0$ as shown in figure 3.3(a). This space was explored by dividing it into a grid of points in steps of $\frac{1}{100}p^t$, $\frac{1}{100}\beta^t$, $\frac{1}{100}\beta^t$. At each point, the method of section 3.2 was used to identify the laminates that could form. This process also identified several lines and surfaces in ($P_3,\ \epsilon^r_{11},\ \epsilon^r_{33}$) space, that were then defined analytically by inspection.

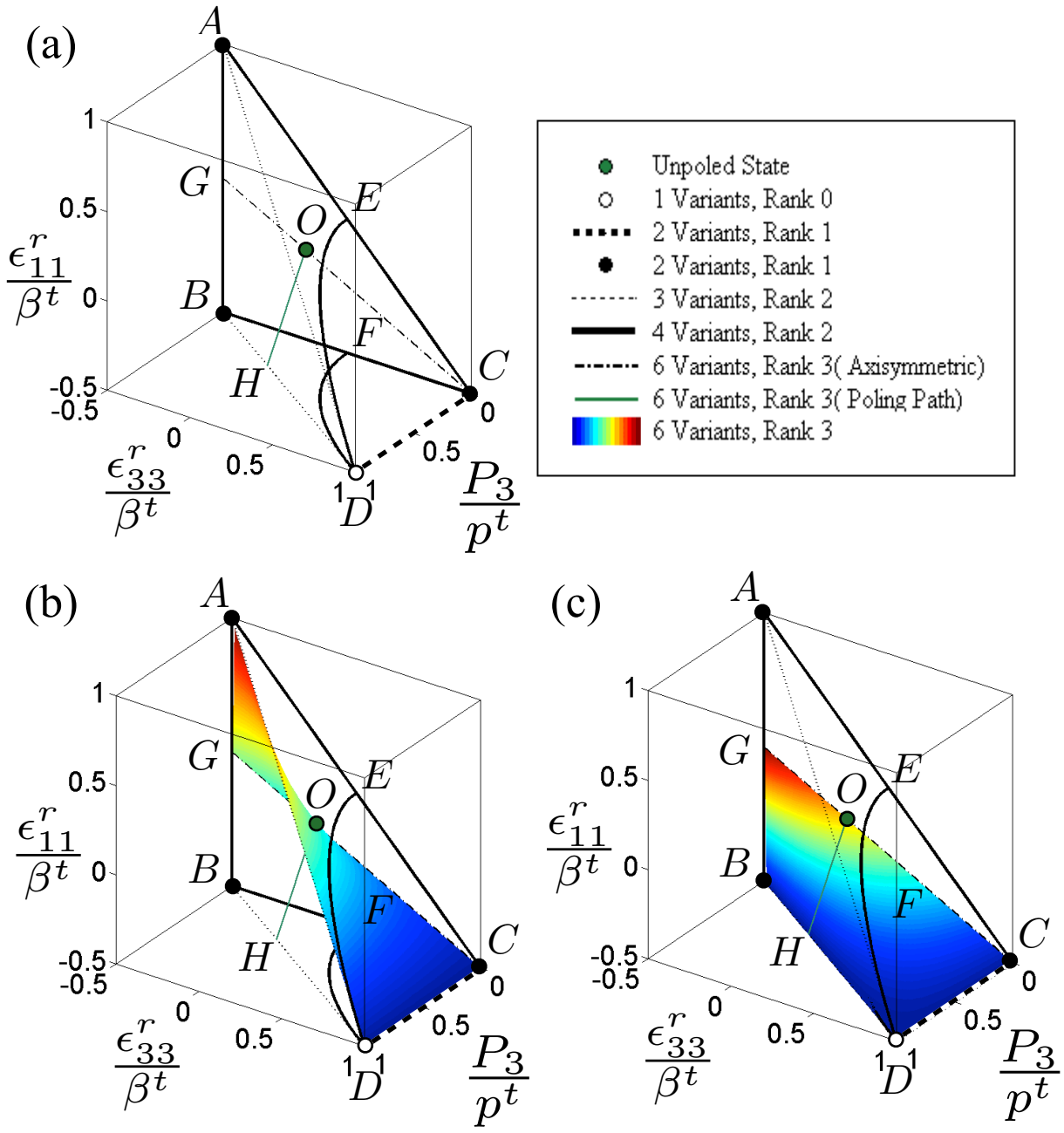

Figure 3.3: (a) The space of possible remanent strain states in a tetragonal single crystal with $P_1 = P_2 = 0$. (b) and (c) illustrate curved spaces of 6 variants rank-3 structures.

The tetrahedral region $ABCD$ in figure 3.3(a) is the possible space of all P_3, ϵ_{11}^r, ϵ_{33}^r values, with the volume fractions constrained by equation (2.14) and by the condition $0 \leq f_{(i)}$. A general point in region $ABCD$ requires all six variants to be present, and so the crystal could form a laminate of rank-3 (minimum possible rank) to rank-5 (Li and Liu's model). However, certain special points in $ABCD$ can have fewer than six variants. Point D represents an ide-

Table 3.2: The crystal variants and volume fraction arrangement on line $\overline{ED}$ (variant numbers in brackets give line $\overline{FD}$) in figure 3.3(a), for the tetragonal crystal system. ($0 < x \leq \frac{1}{4}$ and $\alpha = \frac{(1-2x+\sqrt{1-4x})}{2x}$)

Node	4	5	6	7
Variant	1 (3)	6	5	2 (4)
f_i	x	x/α	αx	x

ally poled state consisting of a single variant (variant number 5 in equation (3.4)) and thus has a rank-0 structure. Points A, B, C and line $\overline{CD}$ everywhere except at D require only two variants, and so a rank-1 structure is possible. The line $\overline{CD}$ represents laminates of variant 5 and variant 6, which have opposite polarization but identical strain; thus the average polarization, P_3, varies along line $\overline{CD}$ without change in the average remanent strain. Points on lines $\overline{AD}$ and $\overline{BD}$ need three variants and form rank-2 exactly compatible structures. Since the cases so far have n variants present with the relationship that $\lceil \log_2 n \rceil = n - 1$, the minimum rank laminates for these points have identical domain configurations to those provided by Li and Liu's model [26]. Typical points in the triangular surfaces ACD and BCD need four variants and rank-3 structures. However, the edges $\overline{AB}$, $\overline{AC}$, $\overline{BC}$ and the curves $\overline{ED}$ and $\overline{FD}$ in figure 3.3(a) comprise a set of strain and polarization states that correspond to rank-2 exactly compatible laminates. The detail of the crystal variants and volume fraction in the lowest level of the tree diagram for points on the curves $\overline{ED}$ and $\overline{FD}$ is shown in table 3.2. By varying the parameter x in the range $0 \leq x \leq 1/4$, all of the polarization and strain states along these curves can be obtained. Two equivalent domain configurations at a typical point on line $\overline{ED}$ are shown in figure 3.4. Figure 3.4(a) shows the structure constructed by the model of Li and Liu, while figure 3.4(b) is one of the constructions of a minimum rank laminate. It can be seen that all the interface orientations of variant pairs in figure 3.4(b) are identical with those in figure 3.4(a).

All remaining points in region $ABCD$ of figure 3.3(a) require at least five variants. These points generally require a lamination of rank-4 or greater and only allow laminate structures that are compatible on average. However, points in the triangle ABC and on the curved surfaces

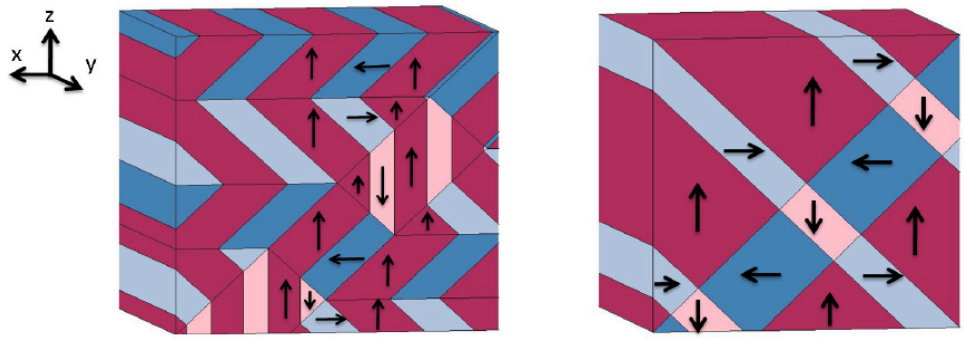

Figure 3.4: Equilibrium microstructures on line $\overline{ED}$ in figure 3.3(a) constructed by (a) rank-3 (method of Li and Liu [26]) (b) rank-2 (the minimum rank.)

Table 3.3: The crystal variants and volume fraction arrangement of surface ABC in figure 3.3, for the tetragonal crystal system. ($0 \leq x \leq \frac{1}{2}$ and $0 \leq y \leq (\frac{1}{2} - x)$, provided that x and y are not zero at the same time. At point O, $x = \frac{1}{12}, y = \frac{1}{6}$)

Node	8	9	10	11	12	13	14	15
Variant	1	2	3	4	2	1	5	6
f_i	x	x	y	y	$\frac{x}{2(x+y)} - x$	$\frac{x}{2(x+y)} - x$	$\frac{y}{2(x+y)} - y$	$\frac{y}{2(x+y)} - y$

$AGCD$ and $GBDC$ (shown in figure 3.3(b), (c)) admit rank-3 exactly compatible structures (see tables 3.3 and 3.4 for details). The curved surfaces $AGCD$ and $GBDC$ contain both the unpoled initial state, O, and the fully-poled state D. Thus *a tetragonal crystal can be poled, while remaining in an exactly compatible state, with laminate structure of rank three or less*. This result implies that tetragonal crystals could be poled by continuous motion of domain walls (without nucleation of new domains) and remain in exactly compatible states that do not necessitate fine domain structure. Thus, some poling paths for tetragonal single crystals can be suggested. For example, the route $O \rightarrow C \rightarrow D$ consists of axisymmetric straining along $\overline{OC}$ ($\epsilon^r_{11} = \epsilon^r_{22} = -\epsilon^r_{33}/2$) as a rank-3 laminate, followed by strain-free 180° switching along $\overline{CD}$. It is interesting to note that the domain configuration jumps two rank levels from rank-3 to rank-1 at point C, where variants 1, 2, 3 and 4 vanish.

It is expected that this poling path could be achieved by a two stage loading process consisting of axisymmetric stress loading, followed by the application of electric field along the

Table 3.4: The crystal variants and volume fraction arrangement of surface $AGCD$(variant numbers in brackets give surface $GBDC$) in figure 3.3, for the tetragonal crystal system. ($0 \leq x \leq 1$, $0 < y \leq \frac{1}{2x+2}$ and $\alpha = \frac{1}{2}\Big(-3y + \sqrt{y^2 + \frac{4y}{1+x}}\ \Big)$. At point O, $x = 1$, $y = \frac{1}{12}$)

Node	8	9	10	11	12	13	14	15
Variant	1 (3)	2 (4)	5	2 (4)	3 (1)	4 (2)	6	4 (2)
f_i	$\alpha + y$	y	$\alpha + \frac{\alpha^2}{y}$	α	$x(\alpha + y)$	xy	$x(\alpha + \frac{\alpha^2}{y})$	$x\alpha$

x_3 direction. The domain evolution during this poling process is shown in figure 3.5. Interestingly, this poling procedure for tetragonal single crystals is similar to a poling method given by Granzow [95] in the context of maximizing polarization in polycrystalline ferroelectrics. An alternative poling path $O \rightarrow H \rightarrow D$ consists of a plane strain deformation, holding $\epsilon^r_{33} = 0$, in rank-3, followed by a second plane strain deformation, holding $\epsilon^r_{11} = -\beta^t/2$, in rank-2. The polarization evolves continuously along this path and so combined stress and electric field boundary conditions could be needed.

Note that the domain configurations corresponding to a given state of strain and polarization are generally nonunique. For example, the unpoled state O in figure 3.3(a) can be realized in many different ways. Three distinct ways can be seen by considering the expressions for the arrangement of nodal volume fractions corresponding to point O in regions ABC, $AGCD$, and $GBDC$ in tables 3.3 and 3.4. It is also worth emphasizing that the compatible solutions found by the present method are restricted to periodic multi-rank laminate configurations. Other compatible configurations can exist, such as the crossing domain patterns identified by Shu and Bhattacharya [24]. Furthermore, non-periodic, or macroscopically inhomogeneous configurations are not considered in this analysis.

Finally, consider disclination-free domain configurations in the tetragonal crystal system. The additional constraint placed on the domain arrangement in order to produce disclination-free structure eliminates all points in region $ABCD$ of figure 3.3(a), except the edges $\overline{AB}$, $\overline{AC}$, $\overline{BC}$ and $\overline{CD}$. Here, disclination-free structures of rank two or less, having pairs of domains with anti-parallel polarization, can be found. Since the unpoled state, O, does not lie within the

set of points where disclination-free structure is possible, there is no disclination-free poling path.

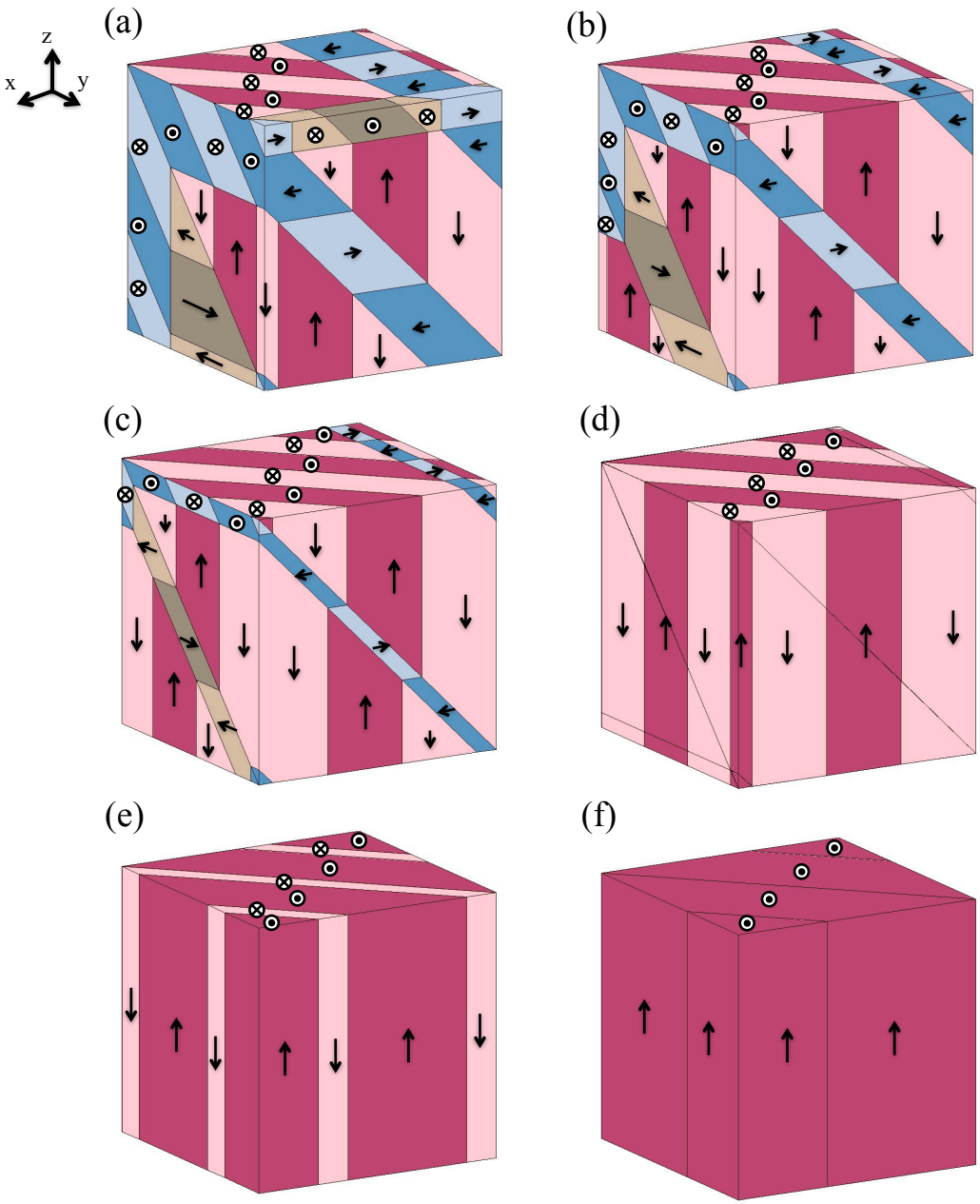

Figure 3.5: The domain evolution in the poling route $O \rightarrow C \rightarrow D$ of figure 3.3 (a) Unpoled state. (b) A typical point on $\overline{OC}$. (c) Variants 1, 2, 3 and 4 vanishing as point C is reached. (d) Rank-1 structure at point C. (e) A typical point on $\overline{CD}$. (f) Fully-poled state.

3.4 Application to rhombohedral ferroelectrics

In the rhombohedral crystal system, there are eight crystal variants with the strain $\boldsymbol{\epsilon}_{(i)}$ and polarization $\mathbf{p}_{(i)},\ (i = 1 \ldots 8)$ are given by

$$\boldsymbol{\epsilon}_{(1,\,2)} = \begin{bmatrix} \alpha^{rh} & \beta^{rh} & \beta^{rh} \\ \beta^{rh} & \alpha^{rh} & \beta^{rh} \\ \beta^{rh} & \beta^{rh} & \alpha^{rh} \end{bmatrix}, \qquad \mathbf{p}_{(1,\,2)} = \pm\tfrac{1}{\sqrt{3}} \begin{bmatrix} p^{rh} \\ p^{rh} \\ p^{rh} \end{bmatrix}$$

$$\boldsymbol{\epsilon}_{(3,\,4)} = \begin{bmatrix} \alpha^{rh} & -\beta^{rh} & -\beta^{rh} \\ -\beta^{rh} & \alpha^{rh} & \beta^{rh} \\ -\beta^{rh} & \beta^{rh} & \alpha^{rh} \end{bmatrix}, \mathbf{p}_{(3,\,4)} = \pm\tfrac{1}{\sqrt{3}} \begin{bmatrix} -p^{rh} \\ p^{rh} \\ p^{rh} \end{bmatrix}$$

$$\boldsymbol{\epsilon}_{(5,\,6)} = \begin{bmatrix} \alpha^{rh} & \beta^{rh} & -\beta^{rh} \\ \beta^{rh} & \alpha^{rh} & -\beta^{rh} \\ -\beta^{rh} & -\beta^{rh} & \alpha^{rh} \end{bmatrix}, \mathbf{p}_{(5,\,6)} = \pm\tfrac{1}{\sqrt{3}} \begin{bmatrix} -p^{rh} \\ -p^{rh} \\ p^{rh} \end{bmatrix} \tag{3.7}$$

$$\boldsymbol{\epsilon}_{(7,\,8)} = \begin{bmatrix} \alpha^{rh} & -\beta^{rh} & \beta^{rh} \\ -\beta^{rh} & \alpha^{rh} & -\beta^{rh} \\ \beta^{rh} & -\beta^{rh} & \alpha^{rh} \end{bmatrix}, \mathbf{p}_{(7,\,8)} = \pm\tfrac{1}{\sqrt{3}} \begin{bmatrix} p^{rh} \\ -p^{rh} \\ p^{rh} \end{bmatrix}$$

Again, α^{rh}, β^{rh} and p^{rh} are material properties; the superscript rh indicates the rhombohedral crystal system. We define the strain states relative to a reference configuration of equal volume, such that $\alpha^{rh} = 0$. Considering disclinations, there are two types of domain walls that contribute to disclinations in the rhombohedral crystal system. The polarization rotations in the rhombohedral system across these two types of domain wall are approximately 71° and 109°.

However, the true rotations $\theta^r(\mathrm{I})$, $\theta^r(\mathrm{II})$ are given by [24]

$$\theta^r(\mathrm{I}) = \cos^{-1}\left(\frac{1-8\beta^{rh}-2\beta^{rh^2}}{3+6\beta^{rh^2}}\right) \tag{3.8}$$

$$\theta^r(\mathrm{II}) = \cos^{-1}\left(-\frac{1+10\beta^{rh}+7\beta^{rh^2}}{3(1+2\beta^{rh}+3\beta^{rh^2})}\right) \tag{3.9}$$

The rotation of lattice planes can be calculated using equation (2.36) and thus the criteria for disclination-free structure can be tested.

For a rhombohedral single crystal with average remanent strain $\boldsymbol{\epsilon}^r$ and average polarization $\mathbf{P}$, equations (2.12)–(2.14) expand into 7 linear equations for the eight unknown volume fractions. The general solution of equations (2.12)–(2.14) gives volume fractions in the form:

$$\begin{bmatrix} f_{(1)} & f_{(2)} & f_{(3)} & f_{(4)} & f_{(5)} & f_{(6)} & f_{(7)} & f_{(8)} \end{bmatrix}^T = \mathbf{x}_0 + \gamma \begin{bmatrix} 1 & -1 & -1 & 1 & 1 & -1 & -1 & 1 \end{bmatrix}^T \tag{3.10}$$

where $\mathbf{x}_0$ is a particular solution and $0 \leq \gamma \leq \gamma_{max}$; the value of γ_{max} is set by the constraint that $0 \leq f_{(i)}$. In the present work, for simplicity, only the cases $\gamma = 0$, $\gamma = \gamma_{max}$ and $\gamma = \gamma_{max}/2$ are considered. When $\gamma = 0$ or γ_{max}, at least one variant has zero volume fraction, and the number of variants present in the laminate is minimised. When $\gamma = \gamma_{max}/2$, the number of variants present is maximized, generally meaning all eight variants are present. This latter choice of γ also maximizes the least volume fraction of any variant and leads to at least two volume fractions being equal.

Now consider the problem of ferroelastic straining of a rhombohedral crystal, maintaining $P_1 = P_2 = P_3 = 0$. The only non-zero strain components are ϵ^r_{12}, ϵ^r_{13} and ϵ^r_{23} and the space of possible strain states is limited to the tetrahedral region $ABCD$ shown in figure 3.6(a). The state O in figure 3.6(a) has $\boldsymbol{\epsilon}^r = \mathbf{0}$ and is representative of a rhombohedral crystal in an unpoled state, as cooled from above the Curie temperature. This point allows several exactly compatible

Table 3.5: The crystal variants and volume fraction arrangement of surfaces $ABDC$, $\epsilon^r_{23} = \epsilon^r_{12}\epsilon^r_{13}$ ($ABCD$, $\epsilon^r_{12} = \epsilon^r_{23}\epsilon^r_{13}$), in figure 3.6, for the rhombohedral crystal system. ($0 \leq x$, $0 \leq y \leq \frac{1}{2x+2}$. At point O, the rank-3 laminate is achieved when $x = 1$, $y = \frac{1}{8}$.)

Node	8	9	10	11	12	13	14	15
Variant	4 (2)	7	3 (1)	8	5 (3)	2 (6)	6 (4)	1 (5)
f_i	$\frac{1}{2x+2} - y$	$\frac{x}{2x+2} - xy$	$\frac{1}{2x+2} - y$	$\frac{x}{2x+2} - xy$	y	xy	y	xy

configurations of either rank-2 or rank-3 with four or eight variants present, respectively. Interestingly, one of the many possible rank-3 laminate solutions at point O (figure 3.7(a)) is identical to the result provided by a recent non-conventional phase field model (figure 3.7(b)) [13]; the detail of the domain arrangement in the lowest level of the tree can be obtained from table 3.5 by setting the parameters $x = 1$, $y = 1/8$. An alternative laminate at point O, of rank-2, is shown in figure 3.7(c); its detail is listed in table 3.6. This domain structure is also identical to the result generated by Shu [22] (figure 3.7(d)).

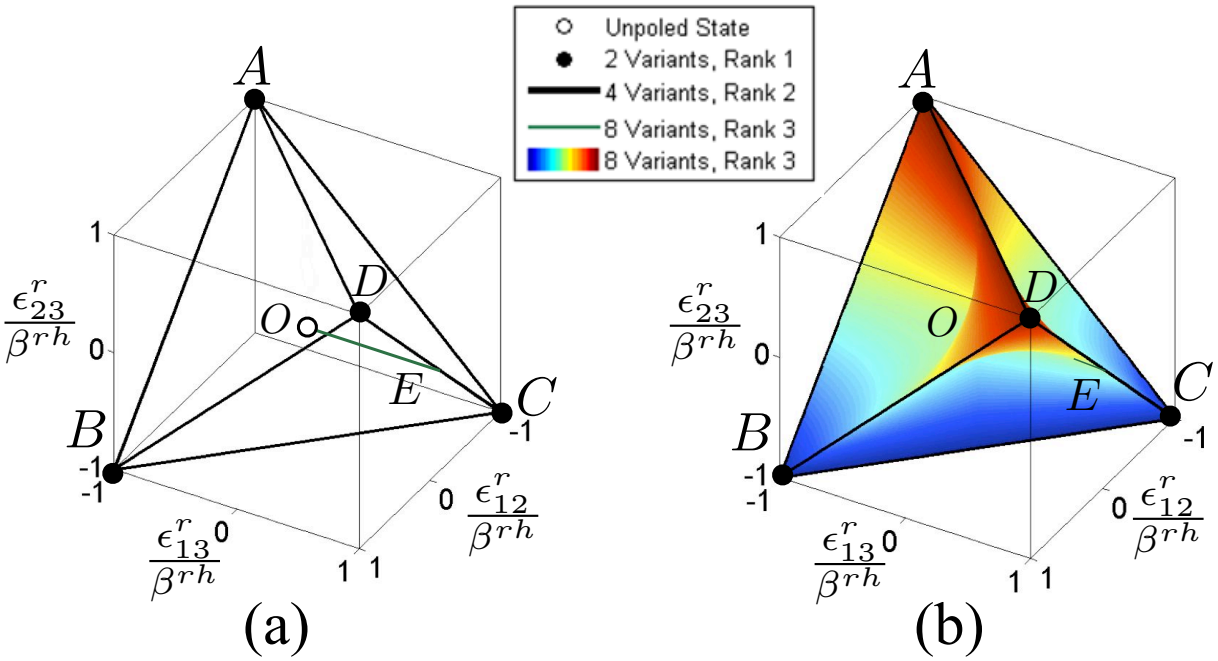

Figure 3.6: The space $ABCD$ of possible remanent strain states in a rhombohedral single crystal with $\mathbf{P} = \mathbf{0}$ (a) Edges and vertices of the tetrahedron, corresponding to structures of rank-2 or less. (b) A curved surface showing the strain states of exactly compatible rank-3 structures with all 8 variants present.

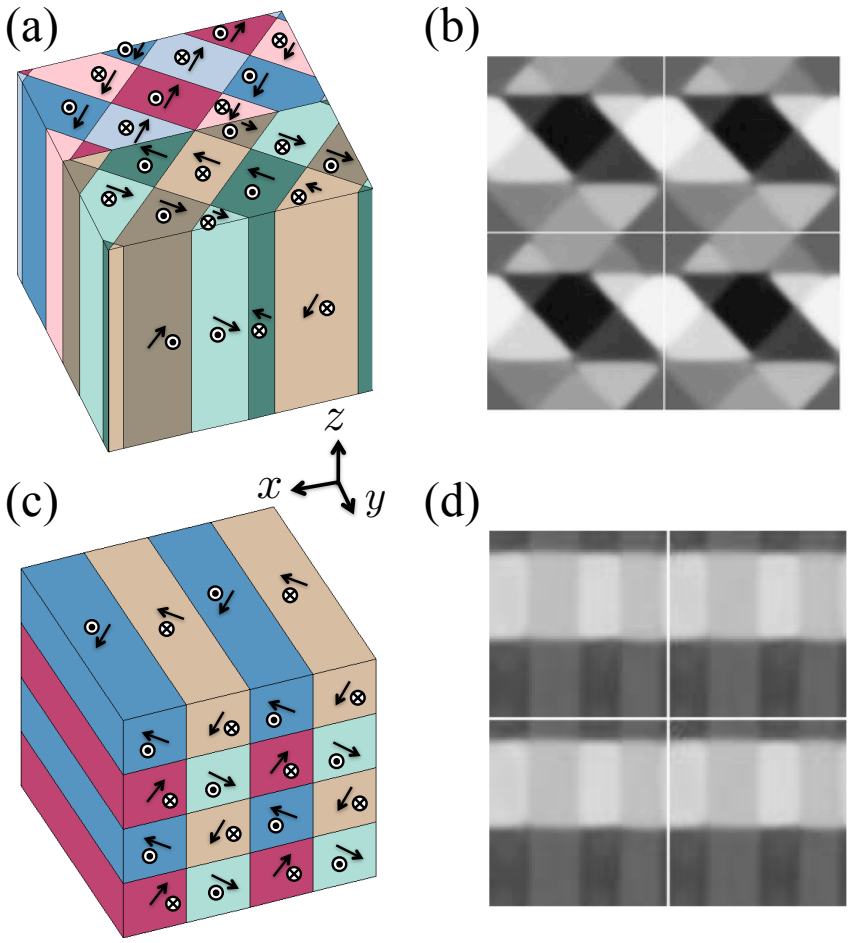

Figure 3.7: (a) One of the possible rank-3 exactly compatible laminates in the unpoled state which is identical to (b) a result provided by Shu *et al.* [13]. (c) An alternative rank-2 exactly compatible laminate in the unpoled state which is also identical to (d) a result generated by Shu [22].

Table 3.6: The crystal variants and volume fraction arrangement of the rank-2 unpoled state O, in figure 3.6, for the rhombohedral crystal system.

Node	4	5	6	7
Variant	1 (2)	4 (3)	5 (6)	8 (7)
f_i	$\frac{1}{4}$	$\frac{1}{4}$	$\frac{1}{4}$	$\frac{1}{4}$

Returning to figure 3.6, points A, B, C, and D require two variants to be present, and allow rank-2 exactly compatible structures. Each of these four points in strain space corresponds to a structure consisting of laminations of a pair of domains with anti-parallel polarization. The six edges $\overline{AB}$, $\overline{AC}$, $\overline{AD}$, $\overline{BC}$, $\overline{BD}$, and $\overline{CD}$ need four variant structures and produce min-

imum rank-2, disclination-free domain configurations. Points on the surfaces ABC, ABD, ACD and BDC require six variants and give rank-3 exactly compatible structures. The points inside region $ABCD$ generally require at least 7 variants and lead to complex configurations of laminate. However, we can find several special cases of minimum rank exactly compatible laminates within $ABCD$. For example, a surface of the form $\epsilon^r_{12} = \epsilon^r_{23}\epsilon^r_{13}$ (and cyclic permutations $\epsilon^r_{23} = \epsilon^r_{12}\epsilon^r_{13}$, $\epsilon^r_{13} = \epsilon^r_{12}\epsilon^r_{23}$) is shown in figure 3.6(b). Points on this surface admit rank-3 exactly compatible structures with all eight variants present (see the detail in table 3.5). The resulting rank-3 laminates do not satisfy the conditions for disclination-free structure; however, it is interesting to note that the angular errors from disclination-free configuration are typically very small (less than 0.01° in $BaTiO_3$) so that the corresponding structures are expected to be low energy configurations. This surface connects the unpoled state, O, with each of the vertices A–D.

As with the tetragonal system, several poling paths for rhombohedral crystals can be suggested which allow the domain configuration to remain in an exactly compatible state with rank three or less. For example, one poling route consists of ferroelastic straining $O \rightarrow E \rightarrow D$ in figure 3.6(a) followed by a strain-free polarizing stage. Stage $O \rightarrow E$ is polarization-free straining, which increases ϵ^r_{23}. The details of domain evolution on $O \rightarrow E$ are given in table 3.5 (region $ABCD$ with $x = 1$ and $1/8 \geq y \geq 0$). This is followed by stage $E \rightarrow D$, comprising further ferroelastic straining with constant ϵ^r_{23}, and $\epsilon^r_{12} = \epsilon^r_{13}$ (see table 3.7 for details). Once point D is reached, the laminate structure has simplified to a rank-1 laminate of variants 1 and 2. This can be poled without further straining by moving the domain wall that separates the two variants. The domain evolution along line $O \rightarrow E \rightarrow D$ and from point D to the fully-poled state is shown in figure 3.8.

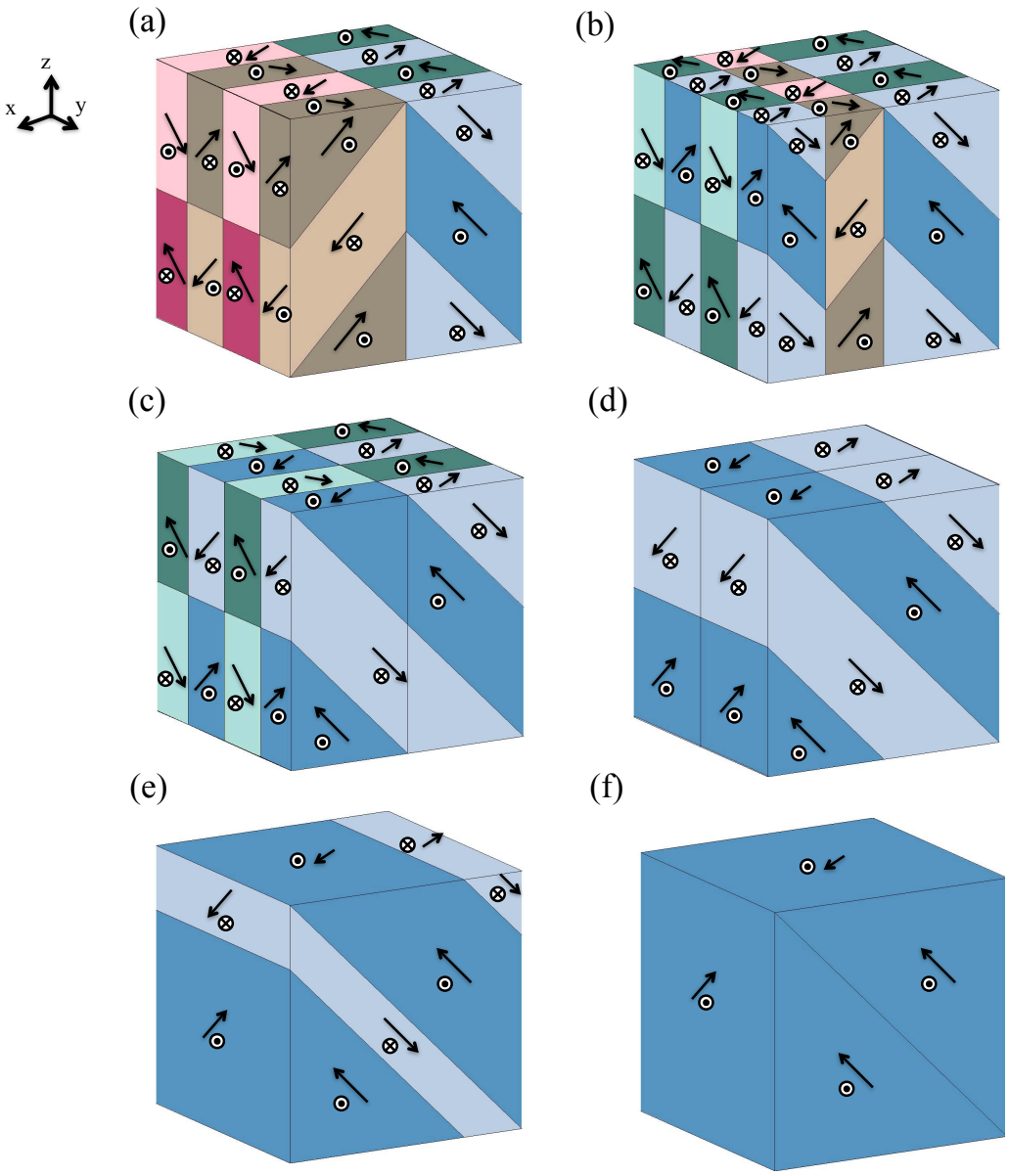

Figure 3.8: The domain evolution in the poling route $O \rightarrow E \rightarrow D$ fully-poled state in figure 3.6. (a) Unpoled state. (b) A typical point on $\overline{OE}$. (c) Rank-2 structure at point E. (d) Rank-1 structure at point D. (e) Rank-1 laminate evolves between point D and fully-poled state. (f) Fully-poled state.

Table 3.7: The crystal variants and volume fraction arrangement of the rank-2 structures on line $\overline{ED}$ in figure 3.6, for the rhombohedral crystal system. ($0 \leq x \leq \frac{1}{4}$)

Node	4	5	6	7
Variant	2	7	1	8
f_i	$\frac{1}{2} - x$	x	$\frac{1}{2} - x$	x

3.5 Classification of laminate domain patterns in ferroelectrics

So far we have found many multi-rank laminate domain structures, such as the well-known herringbone patterns and stripe patterns, which result from twinning to minimise the overall energy of the crystal. These exactly compatible laminate patterns have also been found in many observations [1,2,96], and theoretical models [13,14,22,24,93]. However, given the great number of publications reporting observations of particular domain patterns, it is worth noting that there is up to now no systematic classification of these patterns. What periodic arrangements of domains are possible? What is the relationship between the underlying crystal structure and the domain patterns that form? The answer of these questions is helpful for several reasons: First, it can assist in the interpretation of microstructure observations. For example, images obtained through microscopy give a two-dimensional view and commonly present ambiguity between domain types. Secondly, it is desirable to optimize material properties and structure for applications. A knowledge of the possible domain arrangements could be used to design materials with optimum performance.

The simplicity of the sharp interface models makes it possible to find all of the compatible domain patterns which satisfy a given set of boundary conditions, specified by remanent strain and polarization, as demonstrated in sections 3.3 and 3.4. By removing the boundary conditions altogether, a further step can be taken: the entire set of compatible domain arrangements can be enumerated. Hence an advantage of the constrained theory relative to approaches such as phase field models is the opportunity to obtain an overview of the set of domain patterns that may form. This is the approach pursued in this section, subject to the restriction that only those patterns that can be classified as periodic multi-rank laminates are considered. In order to identify the set of possible laminate domain patterns, the exact compatibility conditions provided in section 2.3.3 are used to determine the compatible arrangements of domains that can form in a given crystal system. This approach is illustrated with a detailed study of rank-2 tetragonal and rhombohedral crystals. Domain structures will be classified and then verified using observations from the

literature and direct observations of barium titanate ($BaTiO_3$) single crystals, obtained courtesy of Mr. P. R. Potnis.

3.5.1 Method for domain structure classification

Consider the problem to find the set of distinct rank-R laminate domain patterns in a given ferroelectric crystal system with k crystal variants. The lowest level of the tree diagram gives $k^{(2^R)}$ possible arrangements. However, as mentioned in section 3.2, permutations that exchange all node pairs in any level of the tree gives identical topology. For a given arrangement of the lowest level of a rank-R tree, there are $2^R - 1$ other identical topologies. For example, a rank-2 domain structure 1234 is equivalent to structures 2143, 3412, 4321. Next remove rigid rotations, reflections and inversions according to the symmetry operations that leave the set of all polarization vectors invariant. For example, figure 3.9 shows that two polar tetragonal domain structures 1234 and 6534 have equivalent domain topologies, since 6534 is a rigid rotation of 1234 by 90° about the y-axis. In the case of sets of crystal variants which are mutually related by pure rotations, the symmetry operations producing equivalent domain topologies are the elements of the $m3m$ symmetry group [97], as shown in table 3.8.

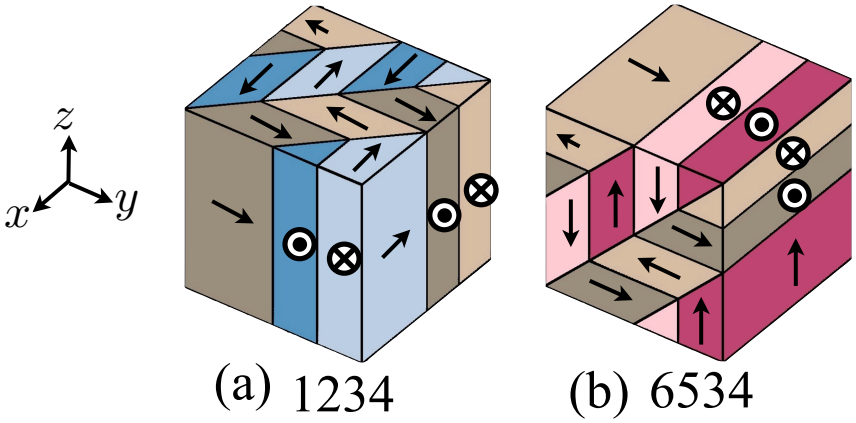

Figure 3.9: Equivalent domain topologies (a) Structure 1234. (b) Structure 6534 is a rigid rotation of 1234 by 90° about the y axis.

Table 3.8: The symmetry operations belonging to the $m3m$ symmetry group.

Symmetry operation	Rotation axes or plane normals
Identity	–
3 axes of 2-fold rotation	$[100]$, $[010]$, $[001]$
6 axes of 4-fold rotation	$[100]$, $[010]$, $[001]$, $[\bar{1}00]$, $[0\bar{1}0]$, $[00\bar{1}]$
6 axes of 2-fold rotation	$[110]$, $[101]$, $[011]$, $[1\bar{1}0]$, $[10\bar{1}]$, $[01\bar{1}]$
8 axes of 3-fold rotation	$[111]$, $[11\bar{1}]$, $[1\bar{1}1]$, $[\bar{1}11]$, $[\bar{1}\bar{1}\bar{1}]$, $[\bar{1}\bar{1}1]$, $[\bar{1}1\bar{1}]$, $[1\bar{1}\bar{1}]$
Inversion	–
3 mirror planes	$[100]$, $[010]$, $[001]$
6 axes of 4-fold rotation with inversion	$[100]$, $[010]$, $[001]$, $[\bar{1}00]$, $[0\bar{1}0]$, $[00\bar{1}]$
6 mirror planes	$[110]$, $[101]$, $[011]$, $[1\bar{1}0]$, $[10\bar{1}]$, $[01\bar{1}]$
8 axes of 3-fold rotation with inversion	$[111]$, $[11\bar{1}]$, $[1\bar{1}1]$, $[\bar{1}11]$, $[\bar{1}\bar{1}\bar{1}]$, $[\bar{1}\bar{1}1]$, $[\bar{1}1\bar{1}]$, $[1\bar{1}\bar{1}]$

We now have the set of crystal variants in the lowest level of the tree diagram which can form distinct topologies. Next we can further identify whether the set of crystal variants can form domain structures which satisfy exact compatibility conditions as provided in section 2.3.3. It is worth to note that exact compatibility condition (i), which requires matching of domain wall spacings, can be achieved by setting the volume fraction of all crystal variants in the lowest level of the tree equal, without losing generality. This is because domain topologies are independent of domain spacing and length scales, as mentioned in section 2.3.1 (see also figure 2.5). Therefore, only conditions (ii) and (iii) of exact compatibility are needed. Conditions (ii) and (iii) give rise to a set of vector equations for determining the interface normals $\mathbf{n}_1 \dots \mathbf{n}_{2^R-1}$. In general, the system of equations is greatly over-constrained. Similar to the solution strategy provided in section 3.2, the degenerate 180° domain walls that give non-unique normal $\mathbf{n}_i$ are dealt with by changing the solution order and using the coplanarity condition, equation (2.31). Solutions exist only for particular combinations of crystal variants. These combinations and their corresponding exactly compatible laminate patterns can then be classified.

Table 3.9: The 24 distinct topologies of a rank-2 laminate made of polar tetragonal crystal variants, showing the subset of eight exactly compatible rank-2 laminates.

Not exactly compatible	Rank < 2, exactly compatible	Rank = 2, exactly compatible
1123	1111	1112
1134	1113	1213
1135	1122	1221
1223	1133	1234
1235	1212	1314
1315	1313	1324
1332	1331	1325
1335		1342
1345		

3.5.2 The set of exactly compatible rank-2 laminates

Here we can apply the procedure for seeking the set of rank-2 laminate structures that can form in a tetragonal ferroelectric crystal. There are six crystal variants, giving $6^4 = 1296$ possible arrangements in the lowest level of the tree diagram. We next remove equivalent domain topologies, such as equivalent permutation of crystal variants and the $m3m$ symmetry. This leaves only the 24 distinct topologies listed in table 3.9. Then the 24 distinct topologies are checked to see if they can satisfy conditions (ii) and (iii). This procedure identifies nine domain topologies that violate the exact compatibility conditions as shown in the first column of table 3.9. Also, seven topologies have all domain walls parallel, and so reduce to laminates of rank less than 2. Finally eight topologies satisfy the exact compatibility conditions and are of rank-2.

Schematic unit cells of these eight types of domain pattern are shown in figure 3.10, where the notation $\{\dots\}$ is used to represent families of symmetry related patterns. It is worth noting that the domain walls marked with dashed lines in figure 3.10 indicate 180° domain walls which can curve to form "watermark" domain patterns. However, some 180° domain walls in figure 3.10 are constrained by the 90° domain walls they meet. This phenomenon was also

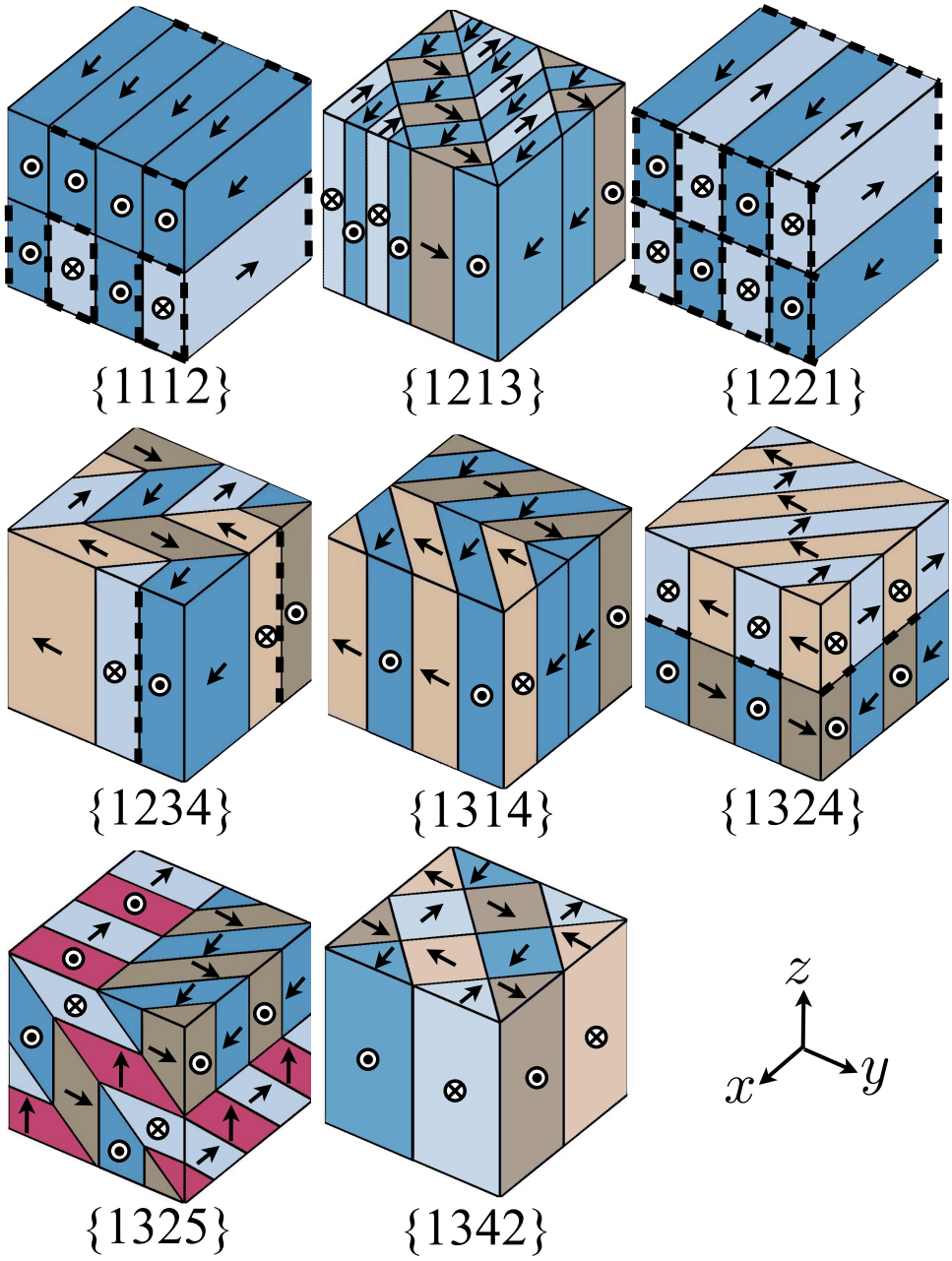

Figure 3.10: Unit cells of the eight exactly compatible, periodic, rank-2 laminate domain patterns in the tetragonal crystal system.

observed by Hu *et al.* [98]. Where the pattern of laminations forces two regions of material of the same crystal variant to meet, there is no domain wall, but fictitious domain walls are included in figure 3.10 to aid visualization of the periodic laminate structure.

The patterns in the $\{1112\}$ and $\{1221\}$ families have only two crystal variants present,

separated by 180° walls. The only distinction between these patterns is whether the domain walls cross, as in $\{1221\}$, or form closed loops, as in $\{1112\}$. It is interesting to note that four families $\{1213\}$, $\{1234\}$, $\{1314\}$ and $\{1325\}$ show herringbone patterns on at least one surface. However all patterns except $\{1325\}$ can show stripes of domains at a surface. This presents considerable ambiguity in identifying domain patterns from surface images. Only family $\{1325\}$ among these eight types has both in-plane and out-of-plane polarization directions present. Thus, the resulting domain structure is the most three-dimensional among the exactly compatible rank-2 laminates. Finally, family $\{1342\}$ takes the form of an array of polarization vortices with alternating sense.

These domain patterns can all be considered as minimum energy states within the constrained theory. However, it is worth noting that the formation of several of the patterns from a high symmetry cubic state results in the presence of disclinations at the junctions of domain walls, i.e. they are not disclination-free domain structures. Using the method provided in section 2.3.5 to check laminate domain patterns for the presence of disclinations, we find that patterns $\{1213\}$ and $\{1314\}$ contain disclinations of magnitude $2(c-a)/a$ at the domain junctions, where a and c are lattice parameters shown in figure 1.1(b); $(c-a)/a$ is a measure of the tetragonality, or distortion of the unit cell away from cubic. Pattern $\{1342\}$ has disclinations of magnitude $4(c-a)/a$. Pattern $\{1325\}$ also has a disclination, though its magnitude is only $\sim 0.86(c-a)^2/a^2$; the other patterns are disclination free. Applying these expressions of disclination magnitude to barium titanate ($BaTiO_3$), the angular errors from disclination-free configuration for patterns $\{1213\}$ and $\{1314\}$ are 1.259°; patterns $\{1342\}$ has disclinations of magnitude about 2.518°; the disclination magnitude of pattern $\{1325\}$ is only 0.006°.

Each of the tetragonal structures shown in figure 3.10 has been reported in the literature, either as the result of direct observation, or from theoretical considerations. In the following paragraphs, evidence for the formation of rank-2 domain structures is given, predominantly by comparing the patterns in figure 3.10 with similar patterns found in the literature. Additionally,

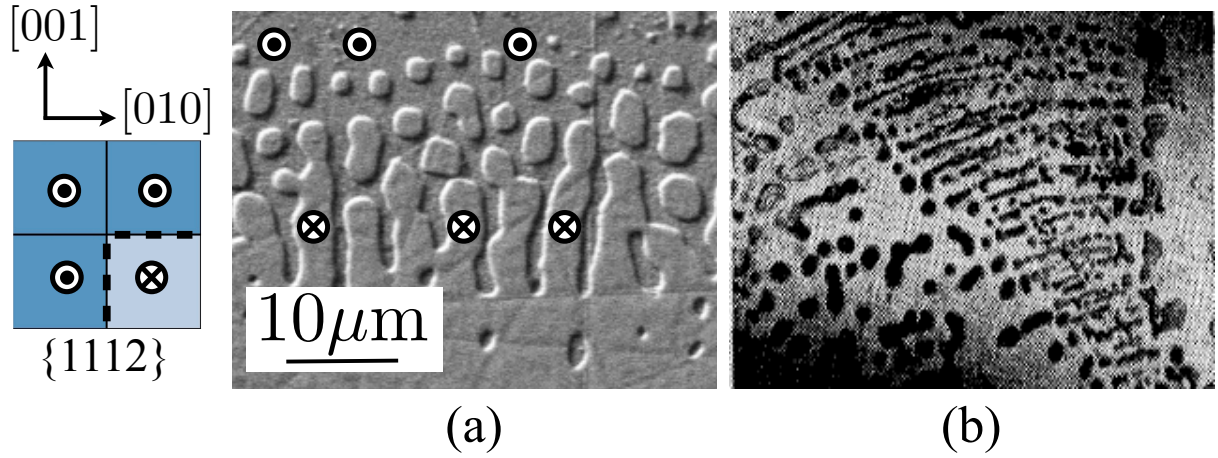

Figure 3.11: Images generated by (a) SEM and (b) optical microscopy [99], showing the $\{1112\}$ rank-2 laminate domain patterns.

examples of several of these structures in an unpoled tetragonal barium titanate single crystal have been found by using a variety of standard imaging techniques, including scanning electron microscopy (SEM), atomic force microscopy (AFM), piezoresponse force microscopy (PFM) and optical microscopy. This experimental data was gathered by my colleague Mr. P. R. Potnis, at University of Oxford, Department of Engineering Science.

Figure 3.11(a) shows a watermark domain pattern with antiparallel out-of-plane polarization directions found in a $BaTiO_3$ single crystal, etched using 10% HF aqueous solution for $20\,\mathrm{s}$. The image was generated using a Zeisss EVO LS 15 ESEM in secondary electron mode, with a $10\,\mathrm{kV}$ beam and $7\,\mathrm{mm}$ working distance. A corresponding surface of the $\{1112\}$ unit cell is shown in the left of figure 3.11. There are several reported observations of $\{1112\}$ type structure [99–101]. Here, an image generated by optical microscopy by Hooton and Merz [99] is also shown in figure 3.11(b). These examples illustrate a $\{1112\}$ type structure in which domain walls are curved. The $\{1221\}$ type structure, however, with crossing $180°$ domain walls, was not found in our crystals. Experimental observations for $\{1221\}$ type appear to be rare and only several illustrations can be found in the literature [102]. A possible explanation is that the crossing domain walls in $\{1221\}$ can separate, merging the regions into closed domain loops, and thus transforming the pattern into the $\{1112\}$ type. This is expected to reduce the overall

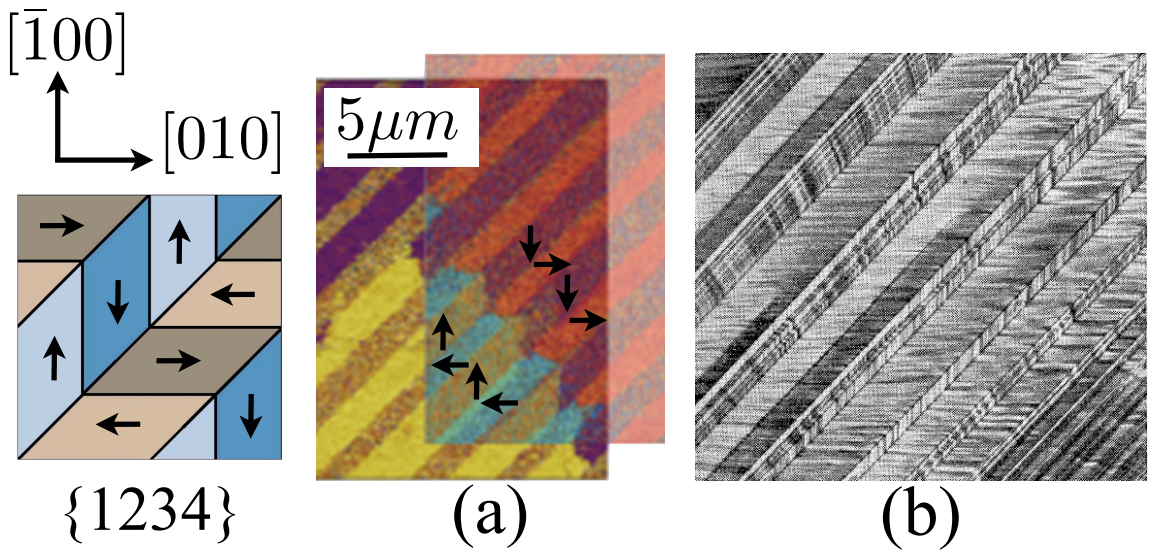

Figure 3.12: Images generated by (a) PFM and (b) optical microscopy [99], showing the $\{1234\}$ rank-2 laminate domain patterns.

domain wall energy by reducing wall area, a factor not considered in the present model.

Figure 3.12(a) shows the domain pattern in an unetched $BaTiO_3$ single crystal, obtained by lateral piezoresponse force microscopy (PFM), that allows mapping of in-plane piezoelectric distortions, and hence the polarization vector direction [103]. An Asylum Research MFP-3D AFM in piezoresponse mode was used, with Olympus AC240TM cantilever. The scan rate was 1 Hz, driving voltage 4.4 V and frequency 885 kHz was used to give contact resonance. In figure 3.12(a), domain pattern $\{1234\}$, with four distinct in-plane domain types in a herringbone arrangement is revealed by overlapping the results from two orthogonal PFM scans. Note that the observed structure cannot be any of the other herringbone patterns as PFM reveals four in-plane domain types. An optical image [99] revealing domain pattern $\{1234\}$ is shown in figure 3.12(b). The $\{1234\}$ structure was also reported in a recent PFM study by McGilly *et al.* [104] and is a well-known arrangement of tetragonal domains [62, 93, 99]

Figure 3.13(a) and (b) show checkerboard domain patterns in etched $BaTiO_3$, imaged by AFM and optical microscopy respectively. The AFM image was obtained using a Veeco Dimension 3100 AFM with Nanoscope IIID Controller. SCM-PIC tips were used in contact mode at a